

An individual star at redshift 1.5 extremely magnified by a galaxy-cluster lens

Patrick L. Kelly¹, Jose M. Diego², Steven Rodney³, Nick Kaiser⁴,
Tom Broadhurst^{5,6}, Adi Zitrin⁷, Tommaso Treu⁸,
Pablo G. Pérez-González⁹, Takahiro Morishita^{8,10,11},
Mathilde Jauzac^{12,13,14}, Jonatan Selsing¹⁵, Masamune Oguri^{16,17,18},
Laurent Pueyo¹⁹, Timothy W. Ross¹, Alexei V. Filippenko¹,
Nathan Smith²⁰, Jens Hjorth¹⁵, S. Bradley Cenko^{21,22}, Xin Wang⁸,
D. Andrew Howell^{23,24}, Johan Richard²⁵, Brenda L. Frye²⁰,
Saurabh W. Jha²⁶, Ryan J. Foley²⁷, Colin Norman²⁸, Marusa Bradac²⁹,
WeiKang Zheng¹, Gabriel Brammer¹⁹, Alberto Molino Benito³⁰,
Antonio Cava³¹, Lise Christensen¹⁵, Selma E. de Mink³²,
Or Graur^{33,34,35}, Claudio Grillo^{36,15}, Ryota Kawamata³⁷,
Jean-Paul Kneib³⁸, Thomas Matheson³⁹, Curtis McCully^{23,24},
Mario Nonino⁴⁰, Ismael Perez-Fournon^{41,42}, Adam G. Riess^{28,19},
Piero Rosati⁴³, Kasper Borello Schmidt⁴⁴, Keren Sharon⁴⁵,
and Benjamin J. Weiner²⁰

¹Department of Astronomy, University of California, Berkeley, CA 94720-3411, USA

²IFCA, Instituto de Física de Cantabria (UC-CSIC), Av. de Los Castros s/n,
39005 Santander, Spain

³Department of Physics and Astronomy, University of South Carolina, 712 Main St.,
Columbia, SC 29208, USA

⁴Institute for Astronomy, University of Hawaii, 2680 Woodlawn Drive, Honolulu,
HI 96822-1839, USA

⁵Department of Theoretical Physics, University of the Basque Country, Bilbao 48080,
Spain

⁶IKERBASQUE, Basque Foundation for Science, Alameda Urquijo, 36-5 48008 Bilbao,
Spain

⁷Physics Department, Ben-Gurion University of the Negev, P.O. Box 653,
Beer-Sheva 8410501, Israel

- ⁸Department of Physics and Astronomy, University of California, Los Angeles, CA 90095
- ⁹Departamento de Astrofísica, Facultad de CC. Físicas,
Universidad Complutense de Madrid, E-28040 Madrid, Spain
- ¹⁰Astronomical Institute, Tohoku University, Aramaki, Aoba, Sendai 980-8578, Japan
- ¹¹Institute for International Advanced Research and Education, Tohoku University,
Aramaki, Aoba, Sendai 980-8578, Japan
- ¹²center for Extragalactic Astronomy, Department of Physics, Durham University,
Durham DH1 3LE, U.K.
- ¹³Institute for Computational Cosmology, Durham University, South Road, Durham DH1
3LE,
U.K.
- ¹⁴Astrophysics and Cosmology Research Unit, School of Mathematical Sciences,
University of KwaZulu-Natal, Durban 4041, South Africa
- ¹⁵Dark Cosmology center, Niels Bohr Institute, University of Copenhagen,
Juliane Maries Vej 30, DK-2100 Copenhagen, Denmark
- ¹⁶Research Center for the Early Universe, University of Tokyo, Tokyo 113-0033, Japan
- ¹⁷Department of Physics, University of Tokyo, 7-3-1 Hongo, Bunkyo-ku, Tokyo 113-0033,
Japan
- ¹⁸Kavli Institute for the Physics and Mathematics of the Universe (Kavli IPMU, WPI),
University of Tokyo, 5-1-5 Kashiwanoha, Kashiwa, Chiba 277-8583, Japan
- ¹⁹Space Telescope Science Institute, 3700 San Martin Dr., Baltimore, MD 21218, USA
- ²⁰Steward Observatory, University of Arizona, 933 N. Cherry Ave., Tucson, AZ 85721,
USA
- ²¹Astrophysics Science Division, NASA Goddard Space Flight Center, Mail Code 661,
Greenbelt, MD 20771, USA
- ²²Joint Space-Science Institute, University of Maryland, College Park, MD 20742, USA
- ²³Las Cumbres Observatory, 6740 Cortona Dr., Suite 102, Goleta, CA 93117, USA
- ²⁴Department of Physics, University of California, Santa Barbara, CA 93106-9530, USA
- ²⁵Univ Lyon, Univ Lyon1, ENS de Lyon, CNRS,
center de Recherche Astrophysique de Lyon UMR5574, F-69230, Saint-Genis-Laval,
France
- ²⁶Department of Physics and Astronomy, Rutgers, The State University of New Jersey,
Piscataway, NJ 08854, USA
- ²⁷Department of Astronomy and Astrophysics, UCO/Lick Observatory,
University of California, 1156 High Street, Santa Cruz, CA 95064, USA
- ²⁸Department of Physics and Astronomy, The Johns Hopkins University,
3400 N. Charles St., Baltimore, MD 21218, USA
- ²⁹Department of Physics, University of California, Davis, 1 Shields Avenue, Davis,
CA 95616, USA
- ³⁰Instituto de Astronomia, Geofísica e Ciências Atmosféricas,
Universidade de São Paulo, 05508-090, São Paulo, Brazil

- ³¹Department of Astronomy, University of Geneva, 51, Ch. des Maillettes,
CH-1290 Versoix, Switzerland
- ³²Anton Pannekoek Institute for Astronomy, University of Amsterdam,
NL-1090 GE Amsterdam, the Netherlands
- ³³Harvard-Smithsonian Center for Astrophysics, 60 Garden Street, Cambridge, MA 02138
- ³⁴Department of Astrophysics, American Museum of Natural History,
Central Park West and 79th Street, New York, NY 10024, USA
- ³⁵NSF Astronomy and Astrophysics Postdoctoral Fellow
- ³⁶Dipartimento di Fisica, Università degli Studi di Milano, via Celoria 16,
I-20133 Milano, Italy
- ³⁷Department of Astronomy, Graduate School of Science, The University of Tokyo,
7-3-1 Hongo, Bunkyo-ku, Tokyo 113-0033, Japan
- ³⁸Laboratoire d’Astrophysique, Ecole Polytechnique Federale de Lausanne (EPFL),
Observatoire de Sauverny, CH-1290 Versoix, Switzerland
- ³⁹National Optical Astronomical Observatory, Tucson, AZ 85719, USA
- ⁴⁰INAF, Osservatorio Astronomico di Trieste, via Bazzoni 2, 34124 Trieste, Italy
- ⁴¹Instituto de Astrofísica de Canarias (IAC), E-38205 La Laguna, Tenerife, Spain
- ⁴²Universidad de La Laguna, Dpto. Astrofísica, E-38206 La Laguna, Tenerife, Spain
- ⁴³Dipartimento di Fisica e Scienze della Terra, Università degli Studi di Ferrara,
via Saragat 1, I-44122, Ferrara, Italy
- ⁴⁴Leibniz-Institut für Astrophysik Potsdam (AIP), An der Sternwarte 16, 14482 Potsdam,
Germany
- ⁴⁵University of Michigan, Department of Astronomy, 1085 South University Avenue,
Ann Arbor, MI 48109-1107, USA

Galaxy-cluster gravitational lenses can magnify background galaxies by a factor of up to ~ 50 . An individual well-aligned background star, however, could potentially become much more highly magnified. Here we report an image of a star (dubbed “MACS J1149 Lensed Star 1 (LS1)”) at redshift $z = 1.49$ magnified by > 2000 . We measure fluctuations in the star’s flux arising from microlensing by intracluster stars and compact objects, whose effective Einstein radii should become exaggerated by a factor of ~ 100 by the cluster’s potential. LS1’s light curve is sensitive to the mass function of intracluster stars and compact objects and provides evidence about

binary fractions as well as specific stellar evolution and supernova models, and against a high abundance of $\sim 30 M_{\odot}$ primordial black holes. A second event, separated by $0.26''$ from LS1, likely corresponds to LS1’s counterimage demagnified for multiple years by a $\gtrsim 3 M_{\odot}$ object in the cluster. Additional monitoring should test the hypothesis that dark matter consists of extremely light bosons.

In *Hubble Space Telescope (HST)* Wide Field Camera 3 (WFC3) infrared (IR) imaging taken on 29 April 2016 to construct light curves of the multiple images of SN Refsdal ($1-10$), we detected a change in flux of a point source (dubbed “MACS J1149 Lensed Star 1 (LS1)”) in the MACS J1149 galaxy-cluster field. As shown in Fig. 1, its position coincides with that of an unresolved blue point source in pre-existing images near the tip of a spiral arm of the host galaxy of SN Refsdal at $z = 1.49$ ($11-14$), and lies within $\sim 0.13''$ of the cluster’s critical curve (CC) ($4-10$).

To characterize the spectral energy distribution (SED) of the transient, we subsequently acquired imaging using the WFC3 and Advanced Camera for Surveys (ACS). As seen in Fig. 2, the excess flux at peak in May 2016 has an SED that is statistically consistent with that of the pre-existing source in archival imaging during 2013–2015. Model spectra of mid-to-late B-type stars at $z = 1.49$ with photospheric temperatures of 11,000–14,000 K (15) provide a good match to the SED of LS1 ($\chi^2 = 12.9$ for 6 degrees of freedom; $\chi^2_{\nu} = 2.15$), given that our model does not account for changes in magnification between observations near peak brightnesses.

Except for finite source effects, lensing magnification should not affect the SED of a magnified star, and a lensed luminous star provides a perhaps surprising – and yet the only explanation – we could find for the transient’s SED and light curve. The spectra of stellar outbursts and supernovae do not show LS1’s strong Balmer break, which indicates a

relatively high surface gravity. Similarly, the temperature of 11,000–14,000 K inferred from fitting the Balmer break is substantially larger than that of almost all H-rich transients such as luminous blue variables (LBVs). LS1 is embedded in an underlying arc that is $\sim 0.2''$ (~ 340 pc) wide, and its stellar population is young with probability peaks at ~ 8 and ~ 35 Myr (see Fig. S1).

In Fig. 3, we display the 2004–2017 light curve of LS1 constructed from all optical and IR *HST* observations of the field. Fig. 3 shows that our simulations of a star experiencing microlensing fluctuations can describe LS1’s light curve, including the May 2016 peak. The May 2016 microlensing event (MACS J1149 Lensing Event (Lev) 2016A) exhibits two statistically significant peaks with potential additional fluctuations, which would correspond to a projected separation for a binary star system of ~ 25 AU for a transverse velocity of 1000 km s^{-1} .

Given LS1’s proximity to the cluster’s CC, we initially considered that a star could be crossing the CC (i.e., caustic in the source plane) (16). Our simulations, however, showed that stars making up the intracluster light (ICL) “disrupt” the cluster’s caustic, leading to many microlensing events corresponding to stars with typical magnifications of $\lesssim 10^4$ instead of a single crossing event with magnification $\sim 10^6$ – 10^7 .

Rest-frame $U - B$ color measures the strength of the Balmer jump, and we searched for blue supergiants in the Magellanic Clouds whose $U - B$ and $B - V$ colors match LS1’s (-0.40 and -0.05 mag, respectively). Almost all luminous stars having similar colors have $M_V \lesssim -8.0$ mag, but the Small Magellanic Cloud has several matching stars with luminosities up to $M_V \gtrsim -8.8$ mag (17).

Current model estimates for the magnification near the CC (4–9) disagree by a factor of ~ 2 . The model we have used for our microlensing analysis predicts that the magnification at LS1’s position should be, on average, ~ 600 per image, and at peak in May 2016, the

star would have been magnified by a factor $\gtrsim 2000$. Assuming that the system comprises of two stars in a binary system having similar luminosities, as indicated by LS1’s light curve, a stellar luminosity of $M_V \approx -8.25$ mag for each star would require a magnification factor of 600 during the period from 2004 through 2011, when the source had an approximate apparent magnitude of $F125W \approx 28.15$.

As we continued to monitor the MACS J1149 cluster field, we detected an unexpected new source (“Lev 2016B”) on 30 October 2016 at roughly the same distance from the CC as LS1, but on the opposite side, as shown in Fig. 4. We measure magnitudes of $F125W = 25.78 \pm 0.12$ AB and $F160W = 26.16 \pm 0.22$ AB. The $F125W - F160W$ color (which corresponds approximately to rest-frame $V - R$) of the new source is consistent with that of LS1, which has $F125W - F160W = -0.11 \pm 0.10$ mag AB. A foreground gravitational lens made of smoothly distributed matter should form a pair of images of a static background source adjacent to the CC. As shown in Fig. 4, Lev 2016B lies at the location where we would expect LS1’s counterimage given our model. The two possible explanations we consider reasonable are that the new source is either the counterimage of LS1, or a different lensed star with a similar rest-frame optical color.

Only the imaging acquired on 30 October 2016 shows a significant source at Lev 2016B’s position. This means that if Lev 2016B is the counterimage of LS1, it must have been demagnified during observations of the cluster field in 2004–2016. Our simulations plotted in Fig. S6 show that, on the Lev 2016B side of the CC, a massive ($\gtrsim 3 M_\odot$) object can demagnify an image of a star for sufficiently long periods spanning the observations. The cluster potential rearranges microlens’ CCs on the Lev 2016B side in an arrangement that can prevent the formation of bright counterimages. Since stars in the ICL with $\gtrsim 3 M_\odot$ are no longer alive, the object could be a stellar binary system, or a neutron star or black hole (BH).

An alternative possibility is that the CC passes very close to LS1 ($\lesssim 0.06$ pc for a magnification at $0.13''$ of 600), and that the two counterimages of the lensed star have small separation that is not detected in *HST* imaging. In this case, the lensed star system could have a total magnification factor of ~ 5000 and a much lower total luminosity of $M_V \approx -6.5$ mag, and Lev 2016B would correspond to a different star. Nonetheless, our simulations shown in Figs. S4 and S5 suggest it may be unlikely that the lensed star would happen to be sufficiently close to the cluster caustic ($\lesssim 0.06$ pc), or that more than one star is responsible for the two events.

Our Monte Carlo simulations plotted in Figs. S4 and S5 suggest that the probability of detecting a bright ($F125W < 27.7$ mag) magnified image that persists for many years in this specific arc may be 1–3% if the stellar luminosity function is relatively shallow to high stellar luminosities ($\alpha \approx 2$, where the number of stars with luminosity between L and $L + dL$ is proportional to $L^{-\alpha} dL$), similar to that of 30 Doradus in the Large Magellanic Cloud (LMC; see Fig. S4). Massive galaxy-cluster lenses create an average of ~ 4 giant arcs (18), and *HST* has been used to observe several dozen massive cluster fields. Consequently, there appears to be a high probability of observing a field where a luminous star lies adjacent to a caustic, but only if high-redshift lensed galaxies have a shallower average stellar luminosity function than those in the nearby universe.

We simulate LS1’s and Lev 2016B’s light curves at an offset of $0.13''$ from the CC using a Chabrier initial mass function (IMF) (19) and several different models of stellar evolution and core-collapse physics, including “Woosley02” (20), “Fryer12” (21), and “Spera15” (22). We construct two separate mass functions for stars and compact objects assuming that (a) all stars are single and (b) adopting the mass-dependent binary fraction and mass ratios of stars measured in the nearby universe (78). The most massive star that is still living found in the intracluster medium (ICM) at $z = 0.54$ is assumed to have

$M = 1.5 M_{\odot}$.

Next, we step through the simulated light curves of a $R = 300 R_{\odot}$ star to identify the intervals that best match LS1’s light curve. When fitting, the star’s luminosity is a free parameter, and we allow the star’s transverse velocity to vary between 100 and 2000 km s^{-1} . We compute the average χ^2 value for the 150 best matches in each light curve. As shown in Fig. S2, the average χ^2 statistic we measure falls within the expected distribution computed from the faked data constructed from the simulated light curves.

In simulations where we generate fake data, the true model has a χ^2 that is at most 15 greater than the best-fitting model, as shown in Fig. S2. Among models where all stars are single, the Fryer12 model has a χ^2 value that is $\gtrsim 25$ higher than the Woosley02 and Spera15 models. As Table S1 shows, the models where we instead adopt the mass-dependent binary fractions and mass ratios observed in the nearby universe (78) show a greater average χ^2 value than the models where all stars are in single systems. While our analysis does not account for the systematic uncertainty in the magnification or mass density of stars and stellar remnants, it demonstrates that the light-curve data should be able to distinguish among binary fractions and potential models of massive stellar evolution.

A recent suggestion is that a significant fraction of dark matter (DM) may consist of relatively massive ($\sim 30 M_{\odot}$) primordial black holes (PBHs) (23). But hiding LS1’s probable counterimage Lev 2016B for a decade would be improbable if $30 M_{\odot}$ PBHs account for 10% of DM, as Fig. S6 shows. Similarly, fits to LS1’s light curve also provide evidence against the hypothesis that 10% of DM is in the form of $\sim 30 M_{\odot}$ PBHs (see Table S1).

While continuing to monitor the field, we detected a new source at $\sim 4\sigma$ significance (Lev 2017A) on 3 January 2017 with a $0.10''$ offset from Lev 2016B, and on the opposite

side of the CC from LS1. Microlensing peaks of distinct stars clustered at large angular separations would be consistent with predictions for fuzzy DM (FDM). According to this hypothesis, DM consists of a scalar field of extremely low-mass particles ($m \approx 10^{-22}$ eV) with de Broglie wavelengths of ~ 1 kpc (24, 25), and is consistent with satellite-galaxy abundances and galaxy mass profiles (26). Interference patterns (27) should break up the main CC into multiple CCs with distances between them of up to $\sim 0.1''$.

References and Notes

1. P. L. Kelly *et al.*, *Science* **347**, 1123–1126 (2015).
2. S. A. Rodney *et al.*, *ApJ* **820**, 50 (2016).
3. P. L. Kelly *et al.*, *ApJ* **819**, L8 (2016).
4. M. Oguri, *MNRAS* **449**, L86–L89 (2015).
5. K. Sharon, T. L. Johnson, *ApJ* **800**, L26 (2015).
6. J. M. Diego *et al.*, *MNRAS* **456**, 356–365 (2016).
7. M. Jauzac *et al.*, *MNRAS* **457**, 2029–2042 (2016).
8. C. Grillo *et al.*, *ApJ* **822**, 78 (2016).
9. R. Kawamata, M. Oguri, M. Ishigaki, K. Shimasaku, M. Ouchi, *ApJ* **819**, 114 (2016).
10. T. Treu *et al.*, *ApJ* **817**, 60 (2016).
11. G. P. Smith *et al.*, *ApJ* **707**, L163–L168 (2009).
12. A. Zitrin, T. Broadhurst, *ApJ* **703**, L132–L136 (2009).
13. T.-T. Yuan, L. J. Kewley, A. M. Swinbank, J. Richard, R. C. Livermore, *ApJ* **732**, L14 (2011).
14. W. Karman *et al.*, *A&A* **585**, A27 (2016).
15. F. Castelli, R. L. Kurucz, *ArXiv Astrophysics e-prints*, eprint: astro-ph/0405087 (2004).
16. J. Miralda-Escude, *ApJ* **379**, 94–98 (1991).
17. J. Dachs, *A&A* **9**, 95–109 (1970).
18. B. Xu *et al.*, *ApJ* **817**, 85 (2016).
19. G. Chabrier, *ApJ* **586**, L133–L136 (2003).

20. S. E. Woosley, A. Heger, T. A. Weaver, *Reviews of Modern Physics* **74**, 1015–1071 (2002).
21. C. L. Fryer *et al.*, *ApJ* **749**, 91 (2012).
22. M. Spera, M. Mapelli, A. Bressan, *MNRAS* **451**, 4086–4103 (2015).
23. S. Bird *et al.*, *Physical Review Letters* **116**, 201301 (2016).
24. L. M. Widrow, N. Kaiser, *ApJ* **416**, L71 (1993).
25. W. Hu, R. Barkana, A. Gruzinov, *Physical Review Letters* **85**, 1158–1161 (2000).
26. L. Hui, J. P. Ostriker, S. Tremaine, E. Witten, *Phys. Rev. D* **95**, 043541 (2017).
27. H.-Y. Schive, T. Chiueh, T. Broadhurst, *Nature Physics* **10**, 496–499 (2014).
28. A. Renzini, L. Ciotti, *ApJ* **416**, L49 (1993).
29. A. Zitrin *et al.*, *ApJ* **801**, 44 (2015).
30. C. Y. Peng, L. C. Ho, C. D. Impey, H.-W. Rix, *AJ* **124**, 266–293 (2002).
31. T. Morishita *et al.*, *ArXiv e-prints*, arXiv: 1610.08503 (2016).
32. M. Kriek *et al.*, *ApJ* **700**, 221–231 (2009).
33. G. Bruzual, S. Charlot, *MNRAS* **344**, 1000–1028 (2003).
34. L. O. V. Edwards, H. S. Alpert, I. L. Trierweiler, T. Abraham, V. G. Beizer, *MNRAS* **461**, 230–239 (2016).
35. W.-R. Hamann, D. Schoenberner, U. Heber, *A&A* **116**, 273–285 (1982).
36. W.-R. Hamann, L. Koesterke, *A&A* **335**, 1003–1008 (1998).
37. N. Smith, *ARA&A* **52**, 487–528 (2014).
38. K. Belczynski *et al.*, *ApJS* **174**, 223–260 (2008).
39. K. Belczynski *et al.*, *ApJ* **714**, 1217–1226 (2010).
40. H. Sana *et al.*, *Science* **337**, 444 (2012).
41. O. Pejcha, T. A. Thompson, *ApJ* **801**, 90 (2015).
42. W. A. Watson *et al.*, *MNRAS* **433**, 1230–1245 (2013).
43. J. M. Lotz *et al.*, *ApJ* **837**, 97 (2017).
44. D. O. Jones, D. M. Scolnic, S. A. Rodney, *PythonPhot: Simple DAOPHOT-type photometry in Python*, Astrophysics Source Code Library, 2015, ascl: 1501.010.
45. S. A. Rodney *et al.*, *ApJ* **811**, 70 (2015).
46. M. Pettini, B. E. J. Pagel, *MNRAS* **348**, L59–L63 (2004).
47. T. Yuan, C. Kobayashi, L. J. Kewley, *ApJ* **804**, L14 (2015).
48. X. Wang *et al.*, *ApJ* **837**, 89 (2017).

49. K. B. Schmidt *et al.*, *ApJ* **782**, L36 (2014).
50. T. Treu *et al.*, *ApJ* **812**, 114 (2015).
51. C. C. Steidel *et al.*, *ApJ* **795**, 165 (2014).
52. P. L. Kelly *et al.*, *ArXiv e-prints*, arXiv: 1512.09093 (2015).
53. R. Maiolino *et al.*, *A&A* **488**, 463–479 (2008).
54. N. Grevesse, A. J. Sauval, *Space Sci. Rev.* **85**, 161–174 (1998).
55. C. Conroy, J. E. Gunn, M. White, *ApJ* **699**, 486–506 (2009).
56. C. Conroy, J. E. Gunn, *ApJ* **712**, 833–857 (2010).
57. P. Kroupa, *MNRAS* **322**, 231–246 (2001).
58. J. A. Cardelli, G. C. Clayton, J. S. Mathis, *ApJ* **345**, 245–256 (1989).
59. P. Marigo, L. Girardi, *A&A* **469**, 239–263 (2007).
60. P. Marigo *et al.*, *A&A* **482**, 883–905 (2008).
61. M. Asplund, N. Grevesse, A. J. Sauval, P. Scott, *ARA&A* **47**, 481–522 (2009).
62. D. Foreman-Mackey, D. W. Hogg, D. Lang, J. Goodman, *PASP* **125**, 306–312 (2013).
63. A. E. Dolphin, *PASP* **112**, 1383–1396 (2000).
64. B. Paczynski, *ApJ* **301**, 503–516 (1986).
65. A. Zitrin *et al.*, *MNRAS* **396**, 1985–2002 (2009).
66. M. Oguri, *PASJ* **62**, 1017–1024 (2010).
67. E. Jullo *et al.*, *New Journal of Physics* **9**, 447 (2007).
68. S. H. Suyu, A. Halkola, *A&A* **524**, A94 (2010).
69. S. H. Suyu *et al.*, *ApJ* **750**, 10 (2012).
70. F. Bresolin *et al.*, *AJ* **116**, 119–130 (1998).
71. W. L. Freedman, *ApJ* **299**, 74–84 (1985).
72. N. Bastian *et al.*, *MNRAS* **379**, 1302–1312 (2007).
73. D. O. Cook *et al.*, *MNRAS* **462**, 3766–3799 (2016).
74. K. Sharon *et al.*, *ApJ* **718**, 876–893 (2010).
75. M. Postman *et al.*, *ApJS* **199**, 25 (2012).
76. A. Kim, A. Goobar, S. Perlmutter, *PASP* **108**, 190 (1996).
77. J. B. Oke *et al.*, *PASP* **107**, 375 (1995).
78. G. Duchêne, A. Kraus, *ARA&A* **51**, 269–310 (2013).

Acknowledgments

We express our appreciation to the Directors of the Space Telescope Science Institute (STScI), the Gemini Observatory, the GTC, and the European Southern Observatory for granting us discretionary time. We thank B. Katz, D. Kushnir, B. Perriello, I. Momcheva, T. Royale, L. Strolger, D. Coe, J. Lotz, M. L. Graham, R. Humphreys, R. Kurucz, A. Dolphin, M. Kriek, S. Rajendran, T. Davis, I. Hubeny, C. Leitherer, F. Nieva, D. Kasen, J. Mauerhan, D. Kelson, J. M. Silverman, and A. Oscoz Abaz. Z. Levay created the color composite image of MACS J1149. The Keck Observatory was made possible by the generous financial support of the W. M. Keck Foundation. Financial support was provided by NASA/STScI grants 14041, 14199, 14208, 14528, 14872, and 14922. P.L.K., A.V.F., and W.Z. are grateful for additional assistance from the Christopher R. Redlich Fund and the TABASGO Foundation. The work of A.V.F. was completed at the Aspen Center for Physics, which is supported by NSF grant PHY-1607611; he thanks the Center for its hospitality during the neutron stars workshop in June and July 2017. J.M.D. acknowledges support of projects AYA2015-64508-P (MINECO/FEDER, UE), AYA2012-39475-C02-01, and the consolidator project CSD2010-00064 funded by the Ministerio de Economía y Competitividad. P.G.P.-G. acknowledges support from Spanish Government MINECO AYA2015-70815-ERC and AYA2015-63650-P Grants. M.O. is supported by JSPS KAKENHI Grant Numbers 26800093 and 15H05892. M.J. acknowledges support by the Science and Technology Facilities Council [grant number ST/L00075X/1]. R.J.F. is supported by NSF grant AST-1518052 and Sloan and Packard Foundation fellowships. M.N. has received support for this work from PRIN-INAF-2014 1.05.01.94.02. O.G. was supported by NSF Fellowship under award AST-1602595.

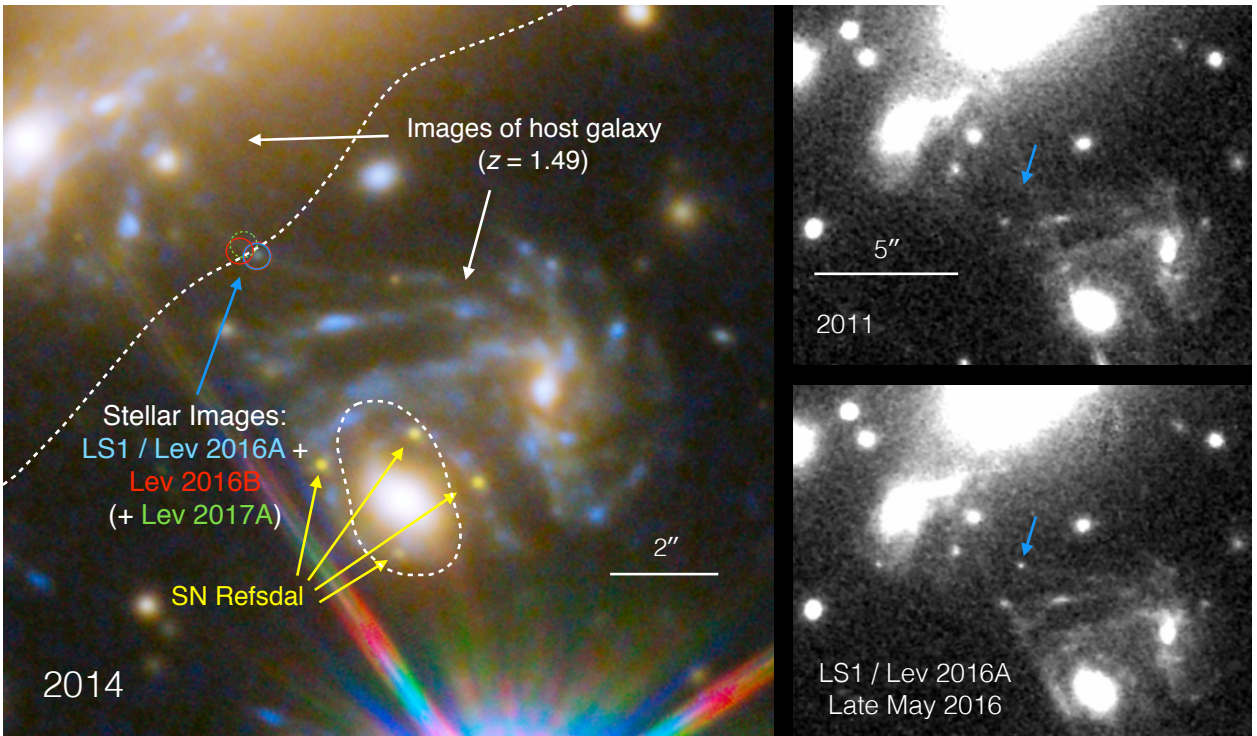


Fig. 1: Left panel shows the positions of magnified images of stars LS1 and Lev 2016B as well as candidate Lev 2017A close to ($\lesssim 0.13''$) the MACS J1149 galaxy cluster's CC, where magnification rises rapidly. Dashed line shows the location of the CC from the CATS cluster model (7). The Einstein cross formed from yellow point sources consists of images of SN Refsdal (1). Right panel shows the field in 2011, and in May 2016 when LS1 exhibited a microlensing peak.

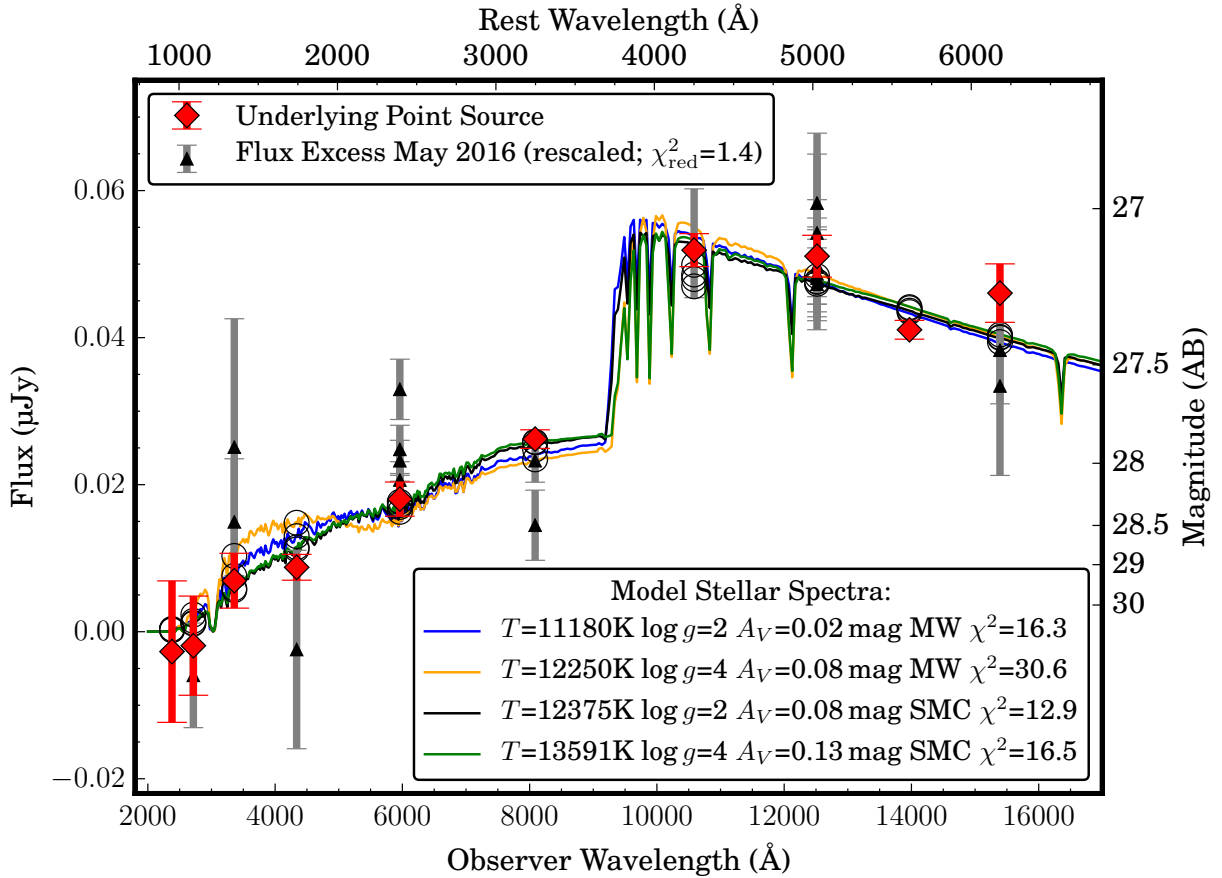


Fig. 2: The SEDs of LS1 in 2011–2015 (black) and of the rescaled, excess flux density at LS1’s position close to its May 2016 peak (Lev 2016A; red). Rescaling the SED of the flux excess to match to that of the 2011–2013 source yields $\chi^2_{\nu} = 1.4$, indicating that they are statistically consistent with each other despite a flux density difference of a factor of ~ 3 –4. The SED shows a strong Balmer break consistent with the host-galaxy redshift of 1.49, and stellar atmosphere models (15) of a mid-to-late B-type star provide a reasonable fit. Black circles show the expected flux density for each model.

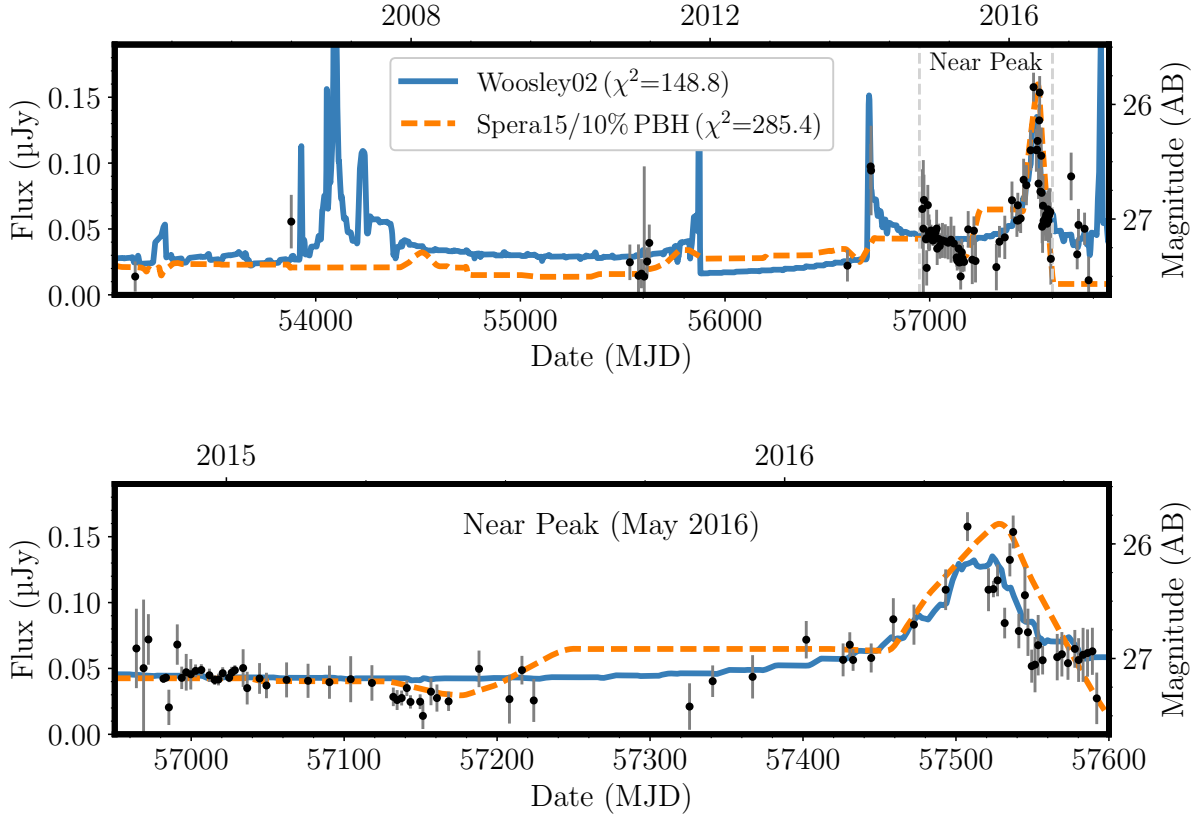


Fig. 3: Light curve of the magnified star LS1, and best-matching simulated light curves during each interval. Fluxes measured through all wide-band *HST* filters are converted to *F125W* using LS1’s SED. Upper panel shows LS1’s full *HST* light curve which begins in 2004. The lower panel shows the most densely sampled part of the light curve including the May 2016 peak (Lev 2016A). This maximum shows two successive peaks that may correspond to a pair of binary companions having similar absolute luminosities. Given the assumed cluster magnification and ICL density, the χ^2 values provide evidence against the Spera15/10%PBH models (see also Table S1).

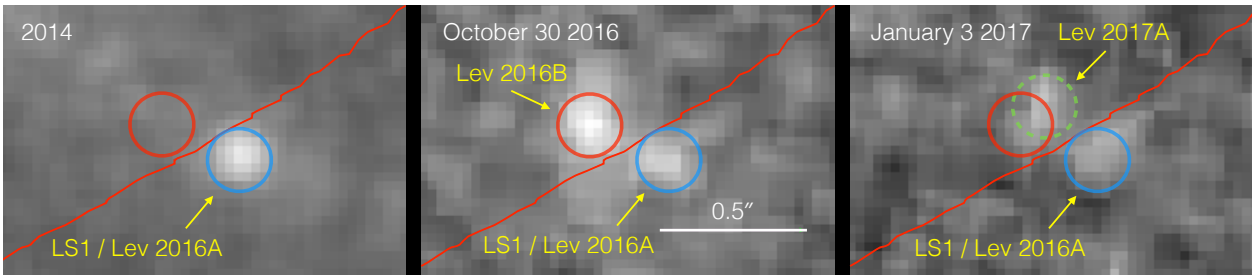


Fig. 4: Successive appearances of highly magnified stellar images near the MACS J1149 galaxy cluster’s CC. The left panel shows LS1 in 2014; we detected LS1 when it temporarily brightened by a factor of ~ 3 in late-April 2016. The center panel shows the appearance of a new image dubbed Lev 2016B on 30 October 2016. The red curve marks the location of the cluster’s CC from the CATS cluster model (7). The position is consistent with the possibility that it is a counterimage of LS1. The right panel shows candidate named Lev 2017A with $\sim 4\sigma$ significance detected on 3 January 2017. If a microlensing peak, Lev 2017A must correspond to a different star.

Supplementary Materials

This PDF file includes the following:

Material and Methods

Supplementary Text

Figs. S1 to S10

Table S1

References 28–77

Materials and Methods

***HST* Imaging.** The *HST* observations include those from GO programs (and Principal Investigators) GO-12065 (M. Postman), 13459 (T.T.), 13504 (J. Lotz), 13790 and 14208 (S.R.), and 14041, 14199, 14528, 14872, and 14922 (P.K.).

Estimate of the Stellar-Mass Density of the ICM. Using *HST* imaging of the MACSJ1149 cluster, we estimate that the mass density of stars and stellar remnants along the line of sight is $6.3_{-3.3}^{+10.3} \times 10^6 M_{\odot} \text{ kpc}^{-2}$, which corresponds to a mass of several $M_{\odot} \text{ pc}^{-2}$ for a Chabrier IMF (19) and the Renzini “initial–final” mass function (28). The total local projected mass density inferred from cluster models (6, 7, 29) is $\log_{10}[\Sigma_{\text{tot}}/(M_{\odot} \text{ kpc}^{-2})] \approx 9.3 \text{ dex}$.

Galaxies with $m_F160W < 26 \text{ AB mag}$ are selected and fit with single Sérsic profiles by using GALFIT (30) in a postage stamp (300 pix \times 300 pix). At the same time, the local sky background, assumed to be constant in the stamp, is fitted with the galaxy light profile simultaneously. After fitting all the galaxies in the field, we reconstruct the ICL map by using the estimated local sky background values. Overlapping pixels are stacked, weighted

by the χ^2_{ν} value of the fit. The uncertainty is estimated from the original root-mean-square (RMS) map (published by the *Hubble* Frontier Fields team) and the systematic differences caused by changing the stamp size. We repeat this procedure for all the *HST* filter bands (31).

Stellar mass is estimated in each pixel by using FAST (32) with the BC03 (33) stellar population model. FAST uses the Galaxy Spectral Evolution Library (GALAXEV; <http://www.bruzual.org/>) code to assemble composite stellar populations. We use the BC03 isochrones, a Chabrier IMF, and an exponentially declining star-formation history. The hot gas in the galaxy-cluster ICM is thought to destroy dust, and extinction from dust is assumed to be zero. We note, however, that setting the dust as a free parameter would change the estimated stellar mass by $< 1\%$.

Mass Function of Surviving Stars and Compact Remnants in Intracluster Medium. For a given a star-formation history, GALAXEV computes the mass in surviving stars and in remnants using the Renzini93 prescription for the mapping between zero-age main-sequence masses and remnant masses (the initial–final mass function) (28). Dead stars with initial masses $M_i < 8.5 M_{\odot}$ become white dwarfs with mass $0.077 M_{\odot} + 0.48 M_i$; those with $8.5 M_{\odot} \leq M_i < 40 M_{\odot}$ become $1.4 M_{\odot}$ neutron stars; and those with $M_i \geq 40 M_{\odot}$ become BHs with $0.5 M_i$.

We assume that the most massive surviving star found in the intracluster medium at $z = 0.54$ has a mass of $1.5 M_{\odot}$, approximately the expected value for a ~ 4.5 Gyr stellar population. For stars with masses $\gtrsim 1.5 M_{\odot}$, we use three separate theoretical initial–final mass functions to compute the distribution of remnant masses.

The evolution of massive stars and the mass of their remnants is expected to depend on the stars’ mass-loss rate, which is thought to vary significantly with their metallicity.

Integral field-unit (IFU) spectroscopy of low-redshift galaxy clusters has been able to place approximate constraints on the metallicity and age of the stars found in the intracluster medium. IFU spectroscopy within ~ 75 kpc of the BCGs of the nearby Abell 85, Abell 2457, and II Zw 108 galaxy clusters found that the ICL light can be best fit by a combination of substantial contributions from an old population (~ 13 Gyr) with high metallicity ($Z \approx 2 Z_{\odot}$) and from a younger population (~ 5 Gyr) with low metallicity ($Z \approx 0.5 Z_{\odot}$) (34).

Stellar Evolution Models. We compute light curves and magnification maps using three sets of predictions for the initial–final mass function (20–22). As a first model, we adopt the initial–final mass function predicted by the solar-metallicity, single stellar evolution models (20) (Woosley02) (Fig. 9 of Ref. 21). In the Woosley02 models, the prescription for driven mass-loss rate at solar metallicity causes stars with initial masses $\gtrsim 33 M_{\odot}$ to end their lives with significantly reduced He core masses, leading such stars to become BH remnants with masses no larger than 5–10 M_{\odot} . The Woosley02 mass-loss prescription uses theoretical models of radiation-driven winds for OB-type stars with $T > 15,000$ K, and empirical estimates for Wolf-Rayet stars (35) that have been adjusted downward by a factor of three to account for the effects of clumping in the stellar wind (36). The mass-loss rate for single O-type stars during their main-sequence evolution may have been overestimated by a factor of 2–3, owing to unmodeled clumping in their winds (37).

A second (Fryer12) initial–final mass function was computed for single stars at subsolar metallicity ($Z = 0.3 Z_{\odot}$; $Z = 0.006$) (Fig. 11 of Ref. 21) as the “DELAYED” curve. These predictions use the StarTrack population synthesis code (38, 39). According to this model, BHs with masses up to 30 M_{\odot} form from the collapse of massive stars.

Finally, we use a third initial–final mass function (Spera15) (Fig. 6 of Ref. 22) to calculate the masses of remnants for the stellar population making up the ICM. The Spera15 relation we adopt was computed using the PARSEC evolution tracks for stars with metallicity $Z = 0.006$, and explosion models where the SN is “delayed,” occurring $\gtrsim 0.5$ s after the initial bounce. According to the Spera15 initial–final mass relation we adopt, stars having initial masses $\gtrsim 33 M_{\odot}$ become BHs with masses within the range 20–50 M_{\odot} . Approximately 70% of massive stars exchange mass with a companion, while $\sim 1/3$ of stars will merge (40). It is also possible that the success of explosions is not related in a simple way to the stars’ initial mass or density structure, given the potentially complex dependence of the critical neutrino luminosity for a successful explosion on these progenitor properties (41).

Transverse Velocity of Star. We use the following expression (Equation 12 of Ref. 16) for the apparent transverse velocity of a lensed source,

$$v_{\perp} = \left| \frac{v_s - v_o}{(1 + z_s)} - \frac{D_s(v_l - v_0)}{D_l(1 + z_l)} \right|, \quad (1)$$

where D_l and D_s are the angular-diameter distances of the lens and source, and v_0 , v_l , and v_s are (respectively) the transverse velocities of the observer, the lens, and the source with respect to the caustic. The expression only applies for a universe without spatial curvature.

Cosmological simulations have found that merging galaxy-cluster halos and subhalos have pairwise velocities of ~ 500 – 1500 km s^{-1} with tails to lower and higher velocity (42). Given the expected velocity of the lens, the peculiar velocities of Earth ($\sim 400 \text{ km s}^{-1}$) and of the host galaxy relative to the Hubble flow, and the motion of the star (< 200 – 300 km s^{-1}) relative to its host galaxy, we adopt 1000 km s^{-1} as a representative transverse velocity. We find, however, that the properties of the simulated light curves do not depend

sensitively on the exact value of the transverse velocity. For a different velocity v in km s^{-1} , the light curve would become stretched by a factor $v/1000$.

Constructing Light Curve. All optical and IR *HST* imaging of the MACS J1149 field with moderate depth has yielded a detection of LS1. For each instrument and wide-band filter combination, we constructed a light curve for LS1. We first measured LS1’s flux in a deep template coaddition of *Hubble* Frontier Fields and early SN Refsdal follow-up imaging. The *Hubble* Frontier Fields program (43) acquired deep imaging of the MACS J1149 galaxy cluster between November 2013 and May 2015 in the ACS WFC $F435W$, $F606W$, and $F814W$ and the WFC3 IR $F105W$, $F125W$, $F140W$, and $F160W$ wide-band filters. The second step was to measure the differences in LS1’s flux between the deep template coadded image and at each imaging epoch. We accomplished this latter step by subtracting the deep template coaddition from coadditions of imaging at each epoch, and measuring the change in LS1’s flux from these resulting difference images.

To measure LS1’s flux in each deep template coaddition, we first fit and then subtracted the ICL surrounding the BCG. We next measured the flux at LS1’s position inside an aperture radius of $r = 0.10''$ using the `PythonPhot` package (44). To measure the uncertainty in the background from the underlying arc, we placed a series of four nonoverlapping apertures having $r = 0.10''$ along it. We use the standard deviation of these aperture fluxes as an estimate of the uncertainty in the background. Aperture corrections were calculated from coadditions of the standard stars P330E and G191B2B (45).

For each *HST* visit, we created a coadded image of all exposures acquired in each wide-band filter. We next subtracted the deep template coaddition from the visit coaddition to create a difference image. Using the `PythonPhot` package (44), we measured the flux inside of a $r = 0.10''$ circular aperture in the difference image. We finally computed the

total flux at each epoch by adding the flux measured from the deep template coaddition and that measured from each difference image.

Estimating LS1’s Color. LS1’s brightness changed between the epochs when the deep template imaging was acquired by the *Hubble* Frontier Fields and SN Refsdal follow-up programs. However, the MACSJ1149 cluster field was monitored using $F125W$ (and $F160W$) with a cadence of ~ 2 weeks after the discovery of SN Refsdal in November 2014 (1). We measured LS1’s $F125W$ light curve from these data, and performed a fit to the light curve using using a third-order polynomial.

We used the polynomial to estimate LS1’s $F125W$ flux at the average epoch when the deep template imaging in each detector and filter was acquired. The ratio between the $F125W$ flux and that in the other filter (e.g., $F140W$) provides a measurement of LS1’s color ($F140W - F125W$, in this example). We restricted the *Hubble* Frontier Fields imaging to that taken between November 2014 and May 2015, since monitoring of SN Refsdal is available to construct LS1’s IR light curve beginning in November 2014.

Creating a Combined Light Curve. We used our estimates of LS1’s color to convert the light curves measured in all available optical and IR filters to $F125W$ light curves, and combined them. We also binned all $F125W$ observations to construct the combined light curve plotted in Fig. 3 and used to fit models.

Metallicity of the Local Host-Galaxy Environment of LS1. The gas-phase oxygen abundance of LS1’s host galaxy, including that within the immediate environment of SN Refsdal, has been studied using multiple datasets. LS1 and SN Refsdal have similar offsets from the host nucleus (within ~ 0.5 kpc), so the local metallicity near LS1’s and SN Refsdal’s host-galaxy locations should have similar values. Both the CATS model

(7) (~ 6.7 kpc and ~ 7.3 kpc, respectively) and the GLAFIC model (9) (~ 7.9 kpc and ~ 8.2 kpc) find similar nuclear offsets for LS1 and SN Refsdal.

Analysis of Keck-II OSIRIS integral-field unit (IFU) spectra reported a 3σ upper limit of $12 + \log(\text{O}/\text{H}) < 8.67$ dex in the Pettini & Pagel N2 calibration (46) for an H II region ~ 200 pc away from SN Refsdal’s site. From the same observations, the authors find a combined upper limit of $12 + \log(\text{O}/\text{H}) < 8.11$ dex from observations of nine H II regions at nuclear offsets between ~ 5 and ~ 7 kpc (47), which is similar to the offsets of LS1 and SN Refsdal.

Recent work (48) has analyzed WFC3 grism spectra taken by GLASS (49, 50) and follow-up observations of SN Refsdal. They fit the abundance measurement using a linear model,

$$12 + \log(\text{O}/\text{H}) = (-0.0666 \pm 0.0232)r + 8.82 \pm 0.039 \text{ dex}, \quad (2)$$

where r is the offset from the nucleus in kpc. This yields an abundance at LS1’s offset (assuming $r = 7.9 \pm 0.5$ kpc) of $12 + \log(\text{O}/\text{H}) = 8.29 \pm 0.19$ dex. This analysis does not take into account the [N II] line when estimating the oxygen abundance, as it can be a biased tracer at $z > 1$ (51).

Finally, while [N II] was not detected in the OSIRIS IFU spectra of the site of SN Refsdal (47), a 1 hr Keck-II MOSFIRE integration yielded a [N II] detection. The [N II] line strength yields a PP04 N2 oxygen abundance of $12 + \log(\text{O}/\text{H}) = 8.3 \pm 0.1$ dex (52), which is in agreement with the above estimate made using the Maiolino calibration (53) from WFC3 grism spectra.

Given the above grism as well as MOSFIRE [N II] metallicity estimates, we use an oxygen abundance of $12 + \log(\text{O}/\text{H}) \approx 8.3$ dex as the metallicity of the massive stellar population near LS1’s coordinates. The Castelli & Kurucz 2004 (15) stellar atmosphere models are parameterised based on the Grevesse & Sauval 1998 (54) solar oxygen abundance

of $12 + \log(\text{O}/\text{H}) = 8.83 \pm 0.06$ dex. Therefore, we adopt $\log(Z/Z_{\odot}) = -0.5$ when drawing comparisons with the Castelli & Kurucz ATLAS9 models.

Constraints on the Age of Stellar Population in Underlying Arc. To compute models using Flexible Stellar Population Synthesis (FSPS) (55, 56), we adopt a simple stellar population with an instantaneous burst of star formation, and include nebular and continuum emission. We use Python bindings (<http://dan.iel.fm/python-fsps/current/>) to FSPS to calculate simple stellar populations with a Kroupa IMF (57) and a Cardelli extinction law with $R_V = 3.1$ (58). These models use the Padova isochrones (59, 60).

A recent analysis finds a solar oxygen abundance of $12 + \log(\text{O}/\text{H}) = 8.69 \pm 0.05$ dex and solar metallicity of $Z = 0.0134$ (61). We therefore calculate models using $\log(Z/Z_{\odot}) = -0.35$, which corresponds to $Z = 0.006$ and is best matched with the FSPS parameter $\text{zmet} = 15$.

To estimate the age and dust extinction of the adjacent stellar population along the arc, we use `emcee` (62), which is an implementation of a Markov Chain Monte Carlo (MCMC) ensemble sampler. We adopt a uniform prior on the stellar population age from 0 to 3 Gyr, and a uniform prior on the extinction A_V from 0 to 2 mag.

Ability to Detect Pair of Images of a Star Adjacent to Cluster Caustic. A possibility is that we do not observe a pair of images of LS1, because it is very close to the cluster caustic and the available *HST* imaging is not able to resolve its two images. Here we calculate how close the star must be to the caustic. If LS1 lay very close to the CC, then Lev 2016B would correspond to the microlensing event of a different star, at an offset of $0.26''$ from the cluster CC.

For a star sufficiently close to the caustic, the pair of images will not be resolved with *HST*. Our simulations suggest that demagnifying one of the two images will be highly

unlikely when the star is close to the cluster caustic. The angular resolution of *HST* is greatest in the *F606W* band and almost as sharp in the *F814W* band, and observations in these wide-band filters provide the best opportunity to test whether LS1 consists of two adjacent images. We use coadditions of imaging taken by the *Hubble* Frontier Fields program. To determine the limit we can place on the separation of two possible images, we inject pairs of point sources having the same combined magnitude as the images made using the ACS WFC *F606W* and ACS WFC *F814W* exposures at each epoch.

The full-width at half-maximum intensity (FWHM) of our ACS point-spread-function (PSF) models constructed from observations of the standard stars P330E and G191B2B only agree within 10% with the measured FWHM of the stars in our coadded images. Consequently, the measured FWHM of the injected pairs of PSFs should not correspond directly to what we would measure in the ACS data. Therefore, we compute the fractional increase in the measured FWHM with the increasing separation between the pair of injected PSFs. Next, we multiply the FWHM estimated from the stars in each image by this factor to compute limits from the ACS imaging.

We inject 100 fake stars with the same magnitude using models of the ACS WFC *F606W* and *F814W* PSF. After injecting the point sources in a grid, we use the IRAF task `imexam` to estimate the Gaussian full-width at half maximum intensity (GFWHM) using the “comma” command from the simulated data. The `imexam` model we use has a Gaussian profile, and we specify three radius adjustments while the fit is optimised. We set the fit radius to be 3 pix ($0.03'' \text{ pix}^{-1}$) and the background buffer to be 5 pix.

These simulations show that any separation between the two images greater than $0.035\text{--}0.040''$ can be detected $> 95\%$ of the time. The upper limit implies that the star would have to be closer than 0.06 pc to the cluster caustic. As we show in Fig. S4, the relative probability of a persistently bright ($F125W < 27.7 \text{ mag}$) star being location within

0.06 pc is $\sim 10\%$.

DOLPHOT (*63*) fit parameters for the images of LS1, Lev 2016B, and Lev 2017A fall in the range expected for point sources in the DOLPHOT reference manual <http://americano.dolphin-sim.com/dolphot/dolphot.pdf>, although these criteria are not highly sensitive to a pair of images.

Interpreting the χ^2 Statistic Using Simulated Light Curves. To determine whether LS1's and Lev 2016B's light curves are able to distinguish among the compact-object remnant populations predicted by the Woosley02, Fryer12, and Spera15 models, as well as the addition of PBHs, we developed a metric based on the χ^2 statistic. We step through the simulated light curves and find the regions that best fit LS1's and Lev 2016B's light curves. We then compute the average χ^2 across the 150 best matches, which we list in Table S1.

To interpret the average χ^2 values, we generate fake light curves for each of the stellar evolution and SN models listed in Table S1 with transverse velocities randomly drawn from a Gaussian distribution centered at 1000 km s^{-1} with a standard deviation of 200 km s^{-1} . We use the cadence and flux uncertainties of the measured light curve of LS1 to generate fake light curves.

All peaks where the peak magnification is between 2000 and 3000 are identified, and we translate the peak of the measured light curve to be aligned with the peak of the model light curve. Next, we sample the model light curve at the point epochs as the shifted empirical light curve, and add Gaussian noise according to the measurement errors. For each such simulated light curve, we compute the average χ^2 statistic using the full set of models. As shown in Fig. S2, the χ^2 statistic we measure for LS1 is consistent with the expected range of values.

For the simulated light curves whose best χ^2 statistic is similar to that we find for LS1 (191.3), the generative (“true”) model never has a χ^2 statistic that exceeds the best-fit χ^2 statistic by more than 15. Consequently, a reasonable conclusion is that the model where PBHs account for 10% of DM are unlikely, given the χ^2 differences listed in Table S1. Under the simple yet unrealistic assumption that no intracluster stars are in binary systems (i.e., Type “S”), the Fryer12 model is also disfavored. Mass functions constructed using the mass-dependent binary fractions observed at low redshift (B) yield greater, yet not significantly larger, χ^2 values than the single-star models (S) for fits to the LS1 light curve. We note that our analysis assumes that the average cluster magnification is 600, and a mass density in surviving stars and compact remnants of $6.3_{-3.3}^{+10.3} \times 10^6 M_\odot \text{ kpc}^{-2}$. Luminous stars can, in many cases, also vary in brightness.

Primordial Black Hole Constraints. As shown in Table S1, our fits to LS1’s light curve disfavor the possibility that PBHs account for $\gtrsim 10\%$ with $M \approx 30 M_\odot$ of galaxy-cluster DM, assuming that the star is located $0.13''$ from the cluster CC. While unlikely given the simulations plotted in Fig. S4, it is also possible that LS1 could be close ($\lesssim 0.06 \text{ pc}$) to the cluster caustic. High optical depth microlensing should yield a bright extended halo close to a large value of surface mass density in microlenses (64).

Supplementary Text

Detection from the Ground with the Gran Telescopio Canarias. We obtained i' -band observations of the MACS J1149 field with the 10.4 m Gran Telescopio Canarias (GTC) on 6 June 2016 and 7 June 2016, after the May 2016 peak. To estimate the flux at LS1’s position, we extracted the flux inside several apertures with diameters within 1–2 times the the PSF FWHM, and applied aperture corrections to obtain integrated

fluxes. The flux estimates for the different apertures agree within 0.10–0.15 mag. The i' -band AB magnitudes are 27.73 ± 0.52 on 57544.9381 MJD in conditions with $1.0''$ seeing and a total integration of 3000 s, and 28.35 ± 0.43 on 57546.9445 MJD in $0.8''$ seeing and a total integration of 5430 s.

Galaxy-Cluster Lens Model. Prior to the identification of LS1 in late-April 2016, the cluster potential had been modeled using the codes LTM (29, 65), WSLAP+ (6), GLAFIC (4, 9, 66), LENSTOOL (5, 7, 67), and GLEE (8, 68, 69). These used several different sets of multiply imaged galaxies (10), which included new data from the Grism-Lensed Survey from Space (GLASS; PI Treu) (49, 50), MUSE (PI Grillo) (8)), and grism follow-up observations of SN Refsdal (PI Kelly) (52).

In Fig. 4, we plot as an example the position of the CC from the CATS model (7) created using LENSTOOL (67), showing that it passes close to the position of LS1. The CCs of all of these models, however, pass within similarly small offsets from LS1’s coordinates.

For the simulation of the light curves of a star passing close to the cluster caustic, we use the WSLAP+ model of the cluster mass distribution (6) and draw stars randomly from a Chabrier IMF (19) until the stellar mass density equals the value we estimate of $6.3_{-3.3}^{+10.3} \times 10^6 M_{\odot} \text{ kpc}^{-2}$.

The WSLAP+ cluster lens model, which includes only smoothly distributed matter and cluster galaxies, yields several important relations describing the magnification near the CC, and the relationship between lensed θ and unlensed β angles. The magnification $\bar{\mu}$ for a smooth cluster model can be described as $\bar{\mu} = 155/\theta$, where θ is the observed angular offset from the CC in arcseconds, and $\bar{\mu} = 19/\sqrt{\beta}$ relates the unlensed angular position β and $\bar{\mu}$. The angles β and θ follow the relation $\beta = \theta^2/66.5$, and both β and θ are in units

of arcseconds.

We simulate the light curves of caustic-crossing events using a resolution of $1 \mu\text{arcsec}$ per pixel over an area of $\sim 83 \text{ pc} \times 6.5 \text{ pc}$ in the lens plane. This area is aligned in the direction where a background source moving toward the cluster caustic would appear to be moving. If the background star is moving with an apparent velocity of 1000 km s^{-1} in the source plane, its associated counterimage would take $\sim 400 \text{ yr}$ to cross the 83 pc of the simulated region. The lensed star is given a transverse velocity of 1000 km s^{-1} in the source plane. Owing to the high magnification, the counterimages’ apparent motion in the image plane is large.

In Fig. S9, we plot magnification maps in the image plane and in the source plane for a model cluster with stars making up the ICL as well as a model cluster that also includes PBHs. For a cluster model populated with stars in the ICM, Fig. S10 shows the “trains” or counterimages that can appear when a lensed star is near the cluster’s caustic. Replacing the cluster’s smoothly varying matter distribution with an increasing fraction of $\sim 30 M_{\odot}$ PBHs yields an increasingly long train, although its expected extent ($\sim 3 \text{ milliarcsec}$) when PBHs account for 10% of DM would be smaller than would be possible to detect in the *HST* imaging. The presence of extended trains for larger PBH abundances, however, helps to explain why it would be difficult to hide LS1’s counterimage for a decade if PBHs account for 10% of DM (see Fig. S6).

Intrinsic Luminosity of Lensed Star. For the inferred photospheric temperature of 11,000–14,000 K and luminosity, the star or pair of stars cannot be on the main sequence. With a redshift time-dilation factor $1 + z = 2.49$, the *HST* monitoring of LS1 from 2004–2017 corresponds to 4.8 yr in the rest frame.

While extremely luminous stars are rare in the nearby universe, they require smaller

magnification and can be at a greater distance from the caustic. For a lens with a smooth distribution of matter, the magnification μ falls within the distance d from the caustic as $\mu \propto 1/\sqrt{d}$. Therefore, the area A in the source plane in which the magnification is greater than μ scales as $A(> \mu) \propto 1/\mu^2$. The observed flux F of a lensed object is $F \propto L\mu$, where the object's luminosity is L . Therefore, a star with luminosity L appears brighter than f inside an area $A(> f; L) \propto L^2$.

Consequently, the probability $p(> f; L)$ that a randomly placed star with luminosity L has a flux brighter than f scales as $p(> f, L) \propto L^2 f(L)$, where $f(L)$ is the stellar luminosity function. If the upper end of the luminosity function is not substantially steeper than L^{-2} , the probability that an observed magnified star is highly luminous may be reasonable, a possibility that we explore quantitatively in the next section.

Probability of Bright Persistent Stellar Image and of Microlensing Events Next to Critical Curve. Gravitational lensing conserves surface brightness, which allows us to use the surface brightness along the CC to estimate the stellar density adjacent to the caustic. First, we calculate the stellar density in the narrow arc (width $\approx 0.2''$) that intersects LS1's location. After subtracting the best-fitting Sérsic model to the BCG, we measure the arc's $F125W$ surface brightness to be $F125W \approx 25 \text{ mag arcsec}^{-2}$.

We calculate that this surface brightness corresponds to a luminosity density of $120 L_{\odot} \text{ pc}^{-2}$, and that the arc's area on the sky within $0.4''$ of the CC corresponds to 7100 pc^2 in the source plane. We renormalise the luminosity function $\psi(L) \propto L^{-\alpha}$, where $\psi(L) dL$ is the number of sources between L and $L + dL$ so that it equals the total luminosity within $0.4''$ of the CC.

We next use Poisson statistics to compute the number of stars in intervals of $0.1 L_{\odot}$. We assign each star a distance from the cluster caustic by randomly drawing from a uniform

probability density function. Massive stars are not uniformly distributed in clusters, but we can expect that this simplification should not be important for estimating the probability of observing at least a single event. However, clustering may be more important for computing the probability of detecting more than a single event. Specifically, luminous, neighboring stars could be responsible for additional events.

We next compute the average magnification of the lensed stars over long periods of time, and their corresponding apparent brightness. At low “optical depth” for microlensing, the cluster model consisting only of smoothly distributed matter should provide a good estimate for average magnification. Where the optical depth for microlensing rises above approximately unity, the lens simulation predicts that the average magnification should differ from that expected from the smooth model. Our simulations show that, near the location of the cluster CC, the magnification reaches 5000 per image. For offsets closer than $0.10''$ to the cluster critical line, we linearly interpolate between the cluster model prediction and 5000 on the critical CC.

We next compute the rate of expected microlensing peaks using a set of simple assumptions (Kaiser et al., in prep.). In the low-optical-depth region, the optical depth for magnification $>\mu$ is

$$f_S(A, \bar{\mu}) \approx 2.5 \times 10^{-4} \left(\frac{\kappa}{3 \times 10^{-3}} \right) \left(\frac{\bar{\mu}}{500} \right)^3 \left(\frac{\mu}{10^4} \right)^{-2}, \quad (3)$$

where μ is the total amplification, κ is the surface density of stars making up the ICL in units of the critical density, and $\bar{\mu}$ is the expected magnification if the cluster consisted entirely of smoothly distributed matter (i.e., in the absence of compact objects).

The quantity $f_S(\mu, \bar{\mu})$ is the fraction of the time that a star reaches a total magnification at least as high as A . While LS1’s light curve shows variation on short- and long-term timescales, its May 2016 peaks lasted only ~ 2 weeks at a flux brighter than

$F_{125W} = 26$ mag AB (although apparently in two successive peaks).

If we count observations of the field taken within 10 days of each other as one observation, then there have been $N = 50$ observations of the field in all optical and IR wide-band filters through 13 April 2017. According to these same criteria, there were $N = 37$ observations through 15 April 2016 just before the detection of LS1.

In Fig. S4, we plot the probability of finding a star with an average F_{125W} brightness of 27.7 mag in the underlying arc as a function of the stellar luminosity function power-law index α . Fig. S4 also shows the probability of observing at least one (as well as at least two) bright ($F_{125W} < 26$ mag) microlensing event(s) given our simple model. Finally, we estimate the probability that the star could be sufficiently close to the galaxy-cluster caustic that its images would be unresolved (< 0.06 pc). The results of our simulation show that the separation of the pair of images follow the relation $4.6\sqrt{t - t_0}$ milliarcsec for a star with a transverse velocity of 1000 km s^{-1} , where t is in years and t_0 is the date when the star crosses the cluster caustic.

For these simulations, we assume that the lensed source is a single star and not a binary star, although Fig. 3 indicates that the Lev 2016A event in May 2016 consists of two successive peaks. Fig. S4 suggests that the probability of observing a persistent bright source may be reasonable, given a shallow stellar luminosity function where $\alpha \approx 2$. Fig. S5 shows the expected distribution of events within $0.4''$ of the CC. Fig. S8 demonstrates that, if a star has an average F_{125W} magnitude of at least 27.7 mag, then it will be responsible for more than $\gtrsim 99\%$ of < 26 mag events. We note, however, that the simulation places stars randomly to reproduce the underlying arc's surface brightness, but luminous stars are not randomly distributed in stellar associations and clusters.

Slope of the Stellar Luminosity Function in Nearby Galaxies. Stars found in OB associations in seven nearby galaxies observed with *HST* show a luminosity function of $\alpha = 2.53 \pm 0.08$ (70). The slope of the stellar luminosity function for stars more luminous than $M_V < -8.5$ mag is not well constrained, but the $\alpha = 2.53 \pm 0.08$ index fit to the full sample of stars with $M_V < -5$ mag (see Fig. 17 of Ref. 70) is consistent with the number counts of stars more luminous than $M_V = -8.5$ mag. This constraint on the power-law index agrees approximately with a separate earlier analysis (71), which studied the slope of the upper end of the stellar luminosity function of the bluest stars in nearby galaxies using ground-based imaging and found $s = 2.68 \pm 0.08$, although the latter analysis extended only to $M_V \approx -9.5$ mag (see Fig. 7 of Ref. 71). A second census of the stellar population in galaxy M101 shows that it may host a smaller number of luminous stars with absolute magnitude $-10 \lesssim M_V \lesssim -11$ (.)

The luminosity function of OB associations (72) can be well described by a power-law function having an index $\alpha \approx 2$. The luminosity function of star-forming regions may become flatter in galaxies with higher star-formation rates and star-formation rate densities (73).

Slope of Stellar Luminosity Function in 30 Doradus. We perform an approximate measurement of the stellar luminosity function of bright stars in the H II region 30 Doradus ($d = 49$ kpc). We retrieve stars from SIMBAD (<http://simbad.u-strasbg.fr/simbad/sim-fout>) having V -band magnitudes and within $20'$ of its center (~ 280 pc). We include object classified as stars, and exclude F,G,K, or M type stars unless they are classified as supergiants. Placing stars in 0.5 mag bins by their absolute V -band magnitudes, we measure a power-law index of $\alpha \approx -2$. No correction is applied for crowding, or the binary fraction.

Observations of Similar Cluster Fields with *HST*. Massive galaxy clusters have been the subject of extensive *HST* imaging and grism-spectroscopy campaigns in the last several years, and these need to be taken into account when considering the probability of finding a highly magnified star microlensed by stars making up the ICL. Detecting transients requires at least two separate observing epochs, which is possible only for programs designed with more than a single visit, or when archival imaging is available. In addition to smaller search efforts (74), large programs have been the Cluster Lensing and Supernova survey with *Hubble* (CLASH) (75), the GLASS (49, 50), the *Hubble* Frontier Fields (43), and the Reionization Lensing Cluster Survey (RELICS). Transients in *Hubble* Frontier Fields and GLASS imaging have been subsequently observed by the FrontierSN program.

With a total of 524 orbits, CLASH acquired imaging of 25 galaxy-cluster fields. A search for transients in the CLASH imaging made use of template archival imaging when available. The survey acquired imaging over a period of three months of each cluster field with repeated visits in each filter. For the coadded imaging from all visits, the limiting magnitude was 27.4 AB for ACS *F814W*, and 27 AB for WFC3 *F125W*. The limiting magnitude of transient searches were brighter, since they require subtraction of a template image.

The *Hubble* Frontier Fields program used 140 orbits (total of 840 orbits) to observe each of 6 galaxy-cluster fields. For each cluster, ACS optical and WFC3 IR imaging was taken in two campaigns, each of which lasted for approximately a month. These were separated from each other by a period of ~ 6 months to allow the telescope roll angles to differ by $\sim 180^\circ$, to image a parallel field adjacent to the cluster with the same instruments. In ACS *F814W*, the limiting magnitude of coadded imaging from all visits was 29.1 AB, and in WFC3 *F125W*, the limiting magnitude was 28.6 AB. Since transient searches require

two epochs, the limiting magnitude for searches was brighter.

The probability of observing a luminous star adjacent to a caustic will depend on the number of lensed galaxies that overlap a galaxy cluster’s caustic. For massive clusters, caustic curves coincide with the intracluster light, so magnified stars should exhibit microlensing fluctuations. Earlier work has estimated that a $10^5 L_\odot$ star ($M_V \approx -7.5$ mag) in a giant arc (with $z = 0.7$) and crossing the caustic of cluster Abell 370 ($z = 0.375$), a *Hubble* Frontier Fields target, would remain brighter than $V = 28$ mag for 700 yr, given a V -band limiting magnitude of 28 and a 300 km s^{-1} transverse velocity (16).

A study of *HST* imaging of CLASH galaxy-cluster fields has found that each cluster field contains 4 ± 1 giant arcs with length $\geq 6''$ and length-to-width ratio ≥ 7 (18). Given that the host galaxy of LS1 would not be classified as a giant arc according to these criteria, it is likely that additional galaxies in each field may lie on the cluster caustic. Considering the 25 CLASH and *Hubble* Frontier Fields cluster observations which each contain a significant number of galaxies lying on the cluster caustic, and the results of our Monte Carlo simulations for the single arc underlying LS1, the probability of observing at least one bright magnified star adjacent to a CC should be appreciable.

K-correction and Distance Modulus. We calculate K -corrections following (Equation 2 of Ref. 76),

$$K = 2.5 \times \log_{10}(1 + z) + m_{F125W,\text{syn}}^{\text{AB}} - m_{V,\text{syn}}^{\text{Vega}}, \quad (4)$$

where $z = 1.49$, $m_{F125W,\text{syn}}^{\text{AB}}$ is the WFC3 $F125W$ synthetic magnitude of a redshifted model spectrum, and $m_{V,\text{syn}}^{\text{Vega}}$ is the synthetic Johnson V -band magnitude of the rest-frame model spectrum. Here the K -correction K_{xy} is defined as

$$m_y = M_x + dm + K_{xy}, \quad (5)$$

where m_y is the observer-frame apparent magnitude in the y band, M_x is the rest-frame absolute magnitude in the x band, and dm is the distance modulus. Using the best-fitting spectral models, we calculate $K_{V,F125W} = -1.10$ mag, and adopt $dm = 45.21$ mag at $z = 1.49$ (with no correction for magnification).

Ground-Based Follow-up Campaigns. We observed the field with direct imaging with the Low Resolution Imaging Spectrometer (LRIS) (77) on the Keck-I telescope on 6 May 2016 (PI Filippenko). Director’s Discretionary programs with the GTC (PI Pérez González; GTC2016-052), the Very Large Telescope (PI Selsing; 297.A-5026), Gemini North (PI Kelly; GN-2016A-DD-8), and the Discovery Channel Telescope (PI Cenko) obtained follow-up imaging in optical bandpasses.

	LS1 150 Best Matches (406 years)					Lev 2016B 150 Best Matches (406 years)				
	$\langle\chi^2\rangle$	Model	PBH	$R(R_\odot)$	Type	$\langle\chi^2\rangle$	Model	PBH	$R(R_\odot)$	Type
Best	191.3	Woosley02		300	S	87.3	Spera15		100	B
	193.5	Fryer15		100	S	88.3	Spera15		100	S
	202.6	Spera15		300	S	92.1	Fryer15		100	B
	207.9	Spera15		80	S	95.0	Woosley15		100	S
	211.3	Spera15		100	S	95.0	Woosley15		100	B
	211.4	Woosley15		100	B	99.5	Fryer15		100	S
	213.5	Fryer15		100	B	103.5	Spera15	1%	1000	S
	215.0	Spera15		100	B	105.9	Spera15		300	S
	225.9	Fryer12		300	S	108.4	Woosley02		300	S
	236.6	Woosley15		100	S	108.5	Fryer12		300	S
	307.0	Fryer12	10%	300	S	124.1	Spera15	3%	1000	S
	Worst	348.1	Spera15	10%	300	S	272.6	Spera15	10%	300

Table S1: Comparison between light curves measured at LS1/Lev 2016A’s and Lev 2016B’s positions and those expected given different stellar evolution and supernova models (20–22), with and without binary companions, and where $30 M_\odot$ PBHs account for an increasing fraction of cluster DM. The “Type” column specified whether the stars are single (S), or have the mass-dependent binary fraction and mass ratios of stars determined at low redshift (B) (78). We step through simulated light curves to find the best χ^2 matches, and list the average χ^2 value for the best 150 matches. As shown in Fig. S2, differences in the average χ^2 statistics are significant, which should provide evidence against the hypothesis that $30 M_\odot$ PBHs account for 10% of DM. However, our analysis does not take into account uncertainty in the average magnification or the mass density of stars in the ICL. Comparisons shown are limited to those where we have produced a simulated light curve.

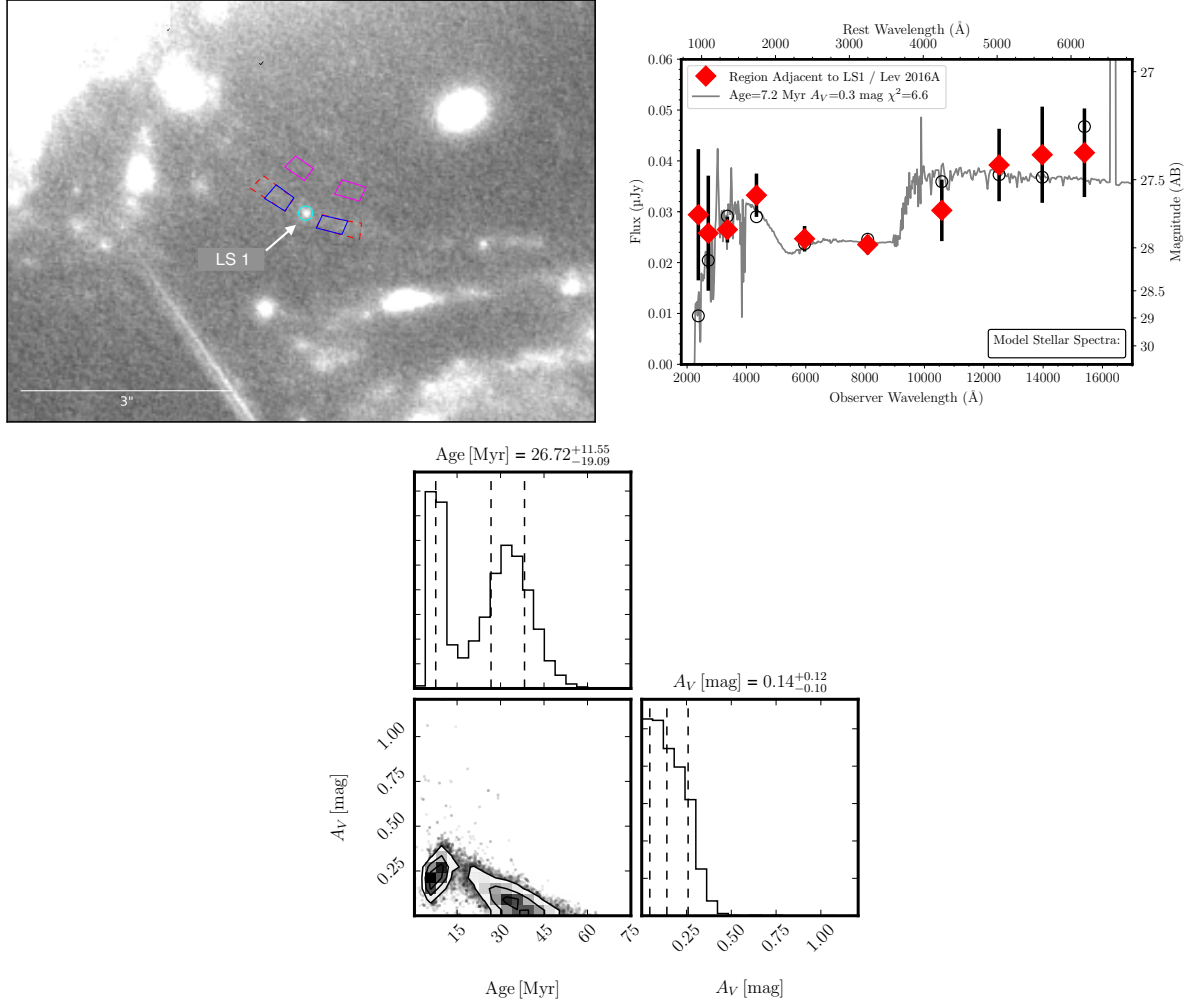


Fig. S1: Constraints on the age and dust extinction of the adjacent stellar population along the lensed arc adjacent to the position of the lensed star LS1. Upper-left panel shows the apertures used to extract photometry of LS1 and arc underlying LS1 superposed on a WFC3 IR $F125W$ image. Cyan circular aperture (radius $r = 0.1''$) was used to extract flux from *Hubble* Frontier Fields imaging, and the background was measured inside of the red dashed aperture. The flux of the arc was measured in the blue solid aperture, and the local background inside of the magenta solid aperture. Upper-right panel plots the SED of the underlying arc measured inside the aperture outlined by a blue boundary. Bottom panel shows the posterior probability distributions of the age and extinction A_V of the stellar population. Spectra of the host galaxy favor a gas-phase metallicity of $Z \approx -0.3$. At such a metallicity, we find a bimodal posterior probability distribution with peaks at ~ 8 and ~ 35 Myr. An age of ~ 8 Myr would be consistent with a blue supergiant star. The stellar population synthesis model is constructed using the Padova isochrones (59, 60), and we apply a Cardelli extinction law with $R_V = 3.1$ (58).

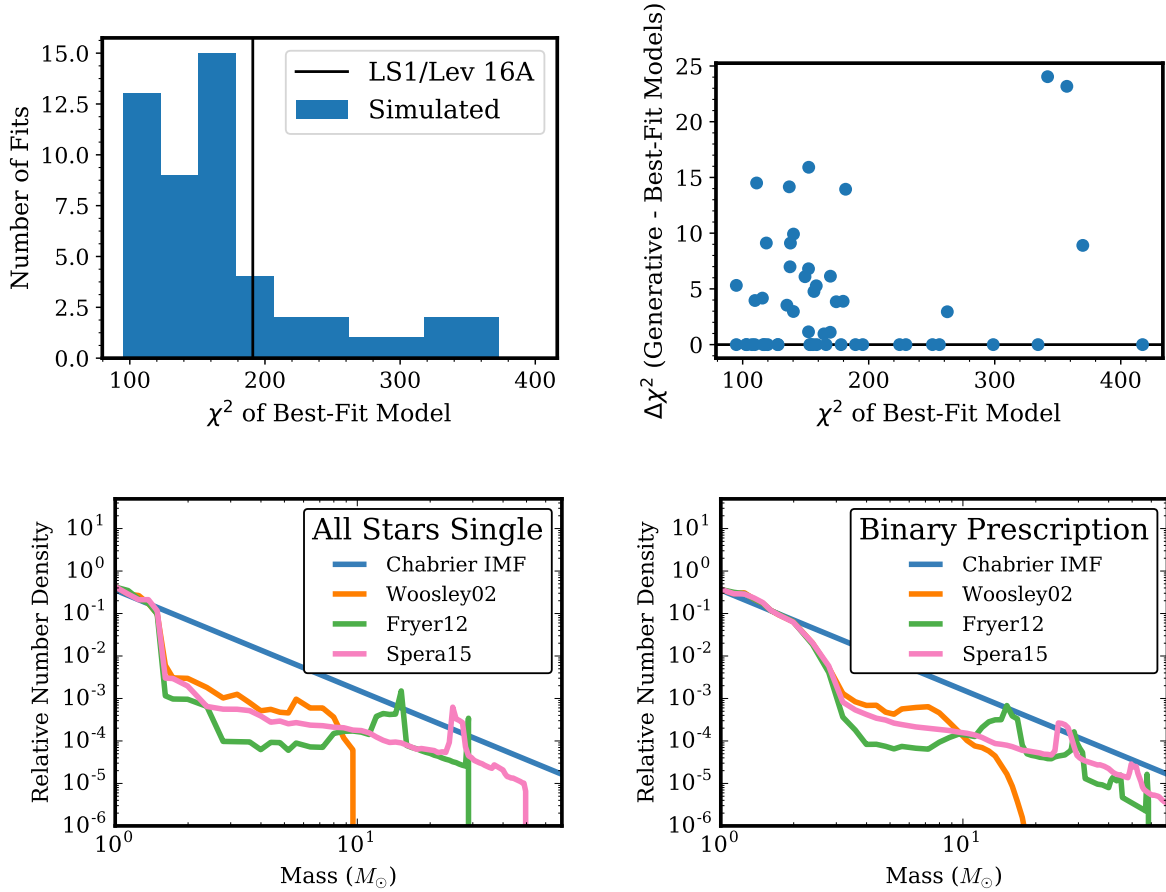


Fig. S2: Simulations of observations and interpretation of χ^2 differences. From simulated light curves, we identify peaks with magnification of 2000–3000, generate fake light curves, and fit these fake data using the full set of simulated light curves. Upper-left panel shows that the best χ^2 we find for LS1 is consistent with the expected distribution of best χ^2 values from the simulations. Upper-right panel demonstrates that, for fake data where the best-chi χ^2 value is close to that observed for LS1 (191.3), the generative (“true”) model used to create the fake data does not have a χ^2 that is more than 15 greater than the χ^2 value of the best-fit model. This implies significant evidence against the Fryer12 and PBH=10% models, given our assumptions about the lens magnification and ICM density. Lower panels show the differences among the mass distributions of surviving stars and stellar remnants (i.e., white dwarf stars, neutron stars, and BHs) for the Woosley02, Fryer12, and Spera15 stellar evolution models, as well as the Chabrier IMF. Lower left plots the mass distributions assuming no stars have companions, and lower right shows mass functions assuming the mass-dependent binary fractions and mass ratios measured at low redshift (78).

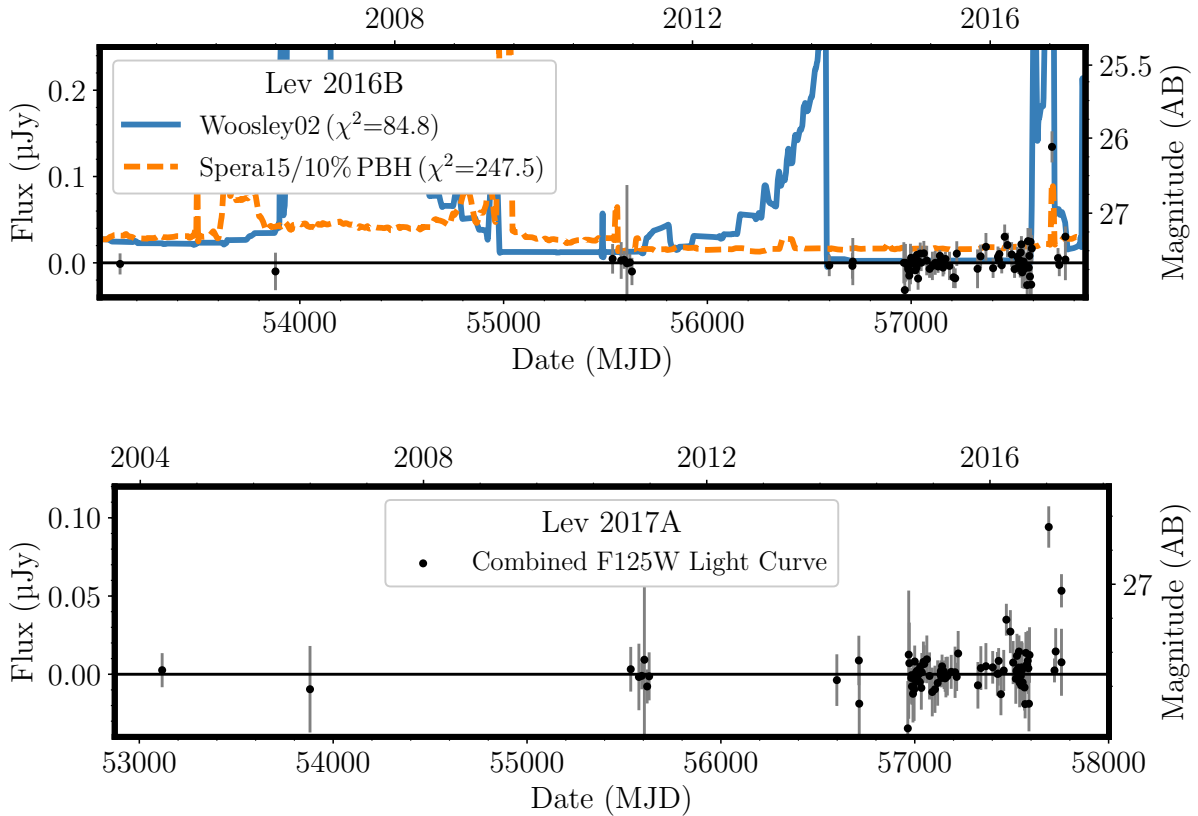


Fig. S3: Light curve in apertures centered on the positions of microlensing events Lev 2016B (upper panel) detected on 30 October 2016 and potential event Lev 2017A (lower panel) detected on 3 January 2017. Fluxes measured through all wide-band *HST* filters are converted to *F125W* using LS1’s SED. Lev 2017A is only offset from Lev 2016B by $0.10''$, so flux measurements at their positions are correlated. The first (higher) peak in Lev 2017A’s light curve plotted here corresponds to flux from Lev 2016B.

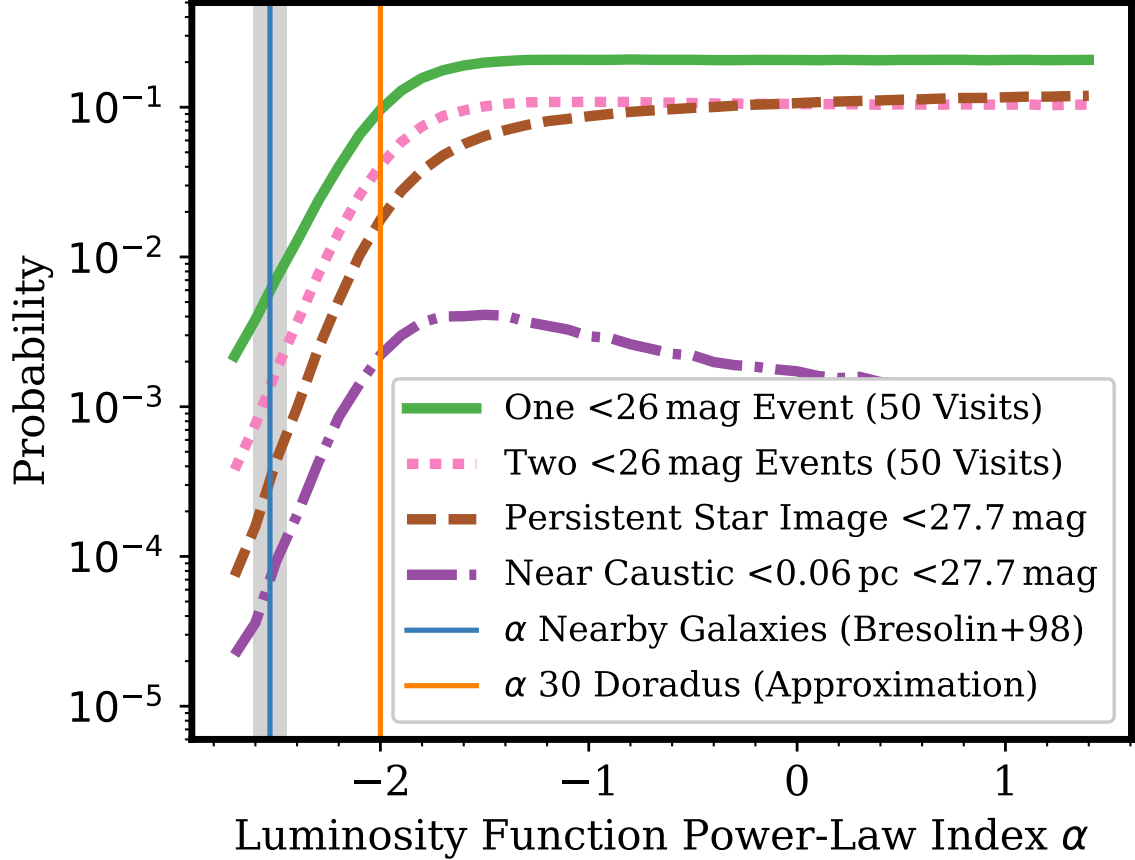


Fig. S4: Effect of the slope of the stellar luminosity function on the probabilities of (a) bright microlensing events ($F_{125W} < 26$ mag; solid green and dotted pink), (b) a persistently bright magnified star ($F_{125W} < 27$ mag) similar to that observed at LS1’s position in 2004–2017 (dashed brown), and (c) a persistently bright magnified star ($F_{125W} < 27$ mag) within 0.06 pc (dot-dash purple). Probabilities are small given the index of stellar luminosity function measured for nearby galaxies ($\alpha = -2.53 \pm 0.08$; vertical blue) (70), but become significantly larger for shallower power-law indices, such as that in the 30 Doradus star-forming region in the LMC (vertical orange). Here we have assumed $N = 37$ visits by *HST*, the number of separate observations of MACS J1149 taken through 13 April 2017 after binning data by 10 days.

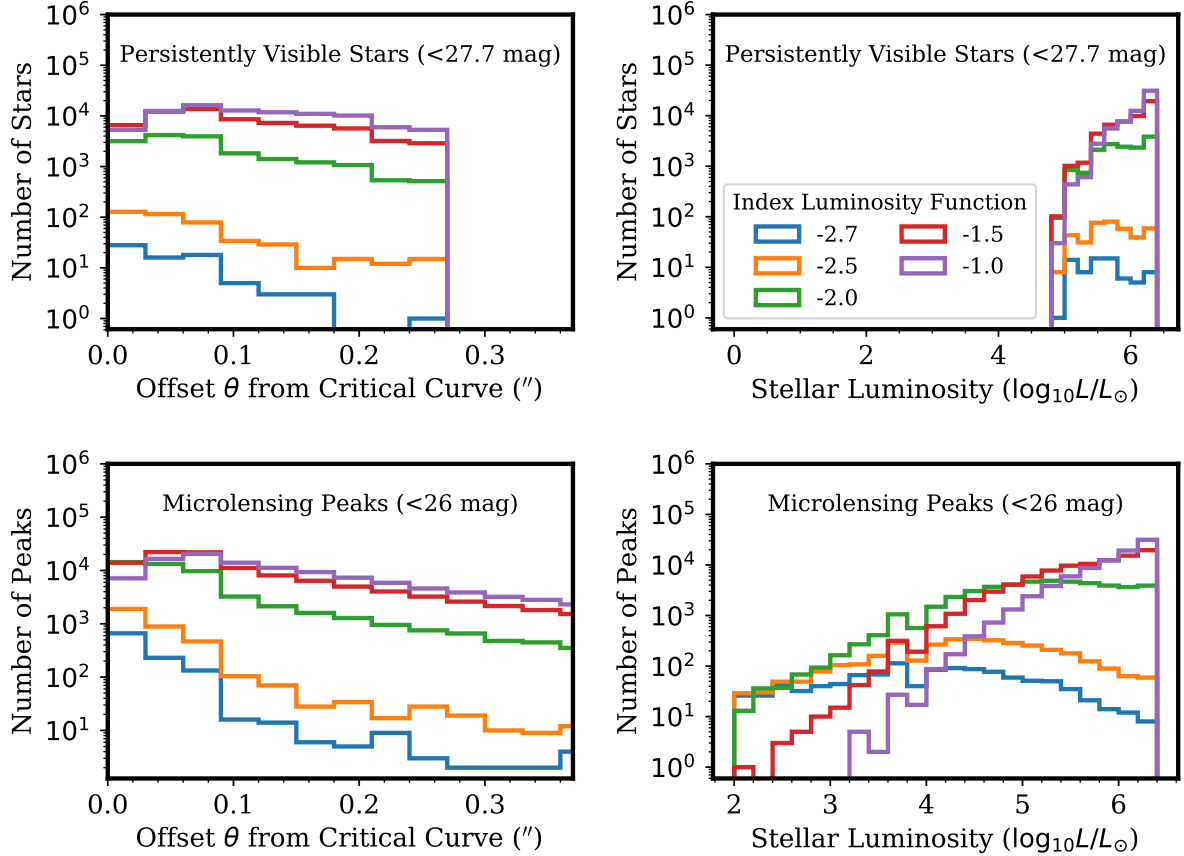


Fig. S5: Results of 10^6 Monte Carlo simulations of stellar population in an underlying arc in the MACS J1149 field for different stellar luminosity functions. We use the surface brightness ($F_{125W} \approx 25 \text{ mag arcsec}^{-2}$) measured along the $0.2''$ -wide arc to constrain the normalisation of the stellar luminosity function, and then Poisson statistics to populate the source plane. Upper panels show that stars with $F_{125W} \leq 27 \text{ mag}$ over a period lasting many years should only appear within $\sim 0.15''$ of the CC, and have luminosities of $\gtrsim 10^{5.4} L_{\odot}$. Lower panels show expected offset distribution of bright microlensing peaks ($F_{125W} \leq 26 \text{ mag}$) to $0.4''$, and of the luminosities of lensed stars. A stellar luminosity function similar to that measured in nearby galaxies ($\alpha = -2.53 \pm 0.08$) yields fewer events with less-luminous stars (70). Left panels indicate the offset θ in arcseconds of stars from the CC, while right panels show the intrinsic luminosity of the stars in units of the solar luminosity (L_{\odot}).

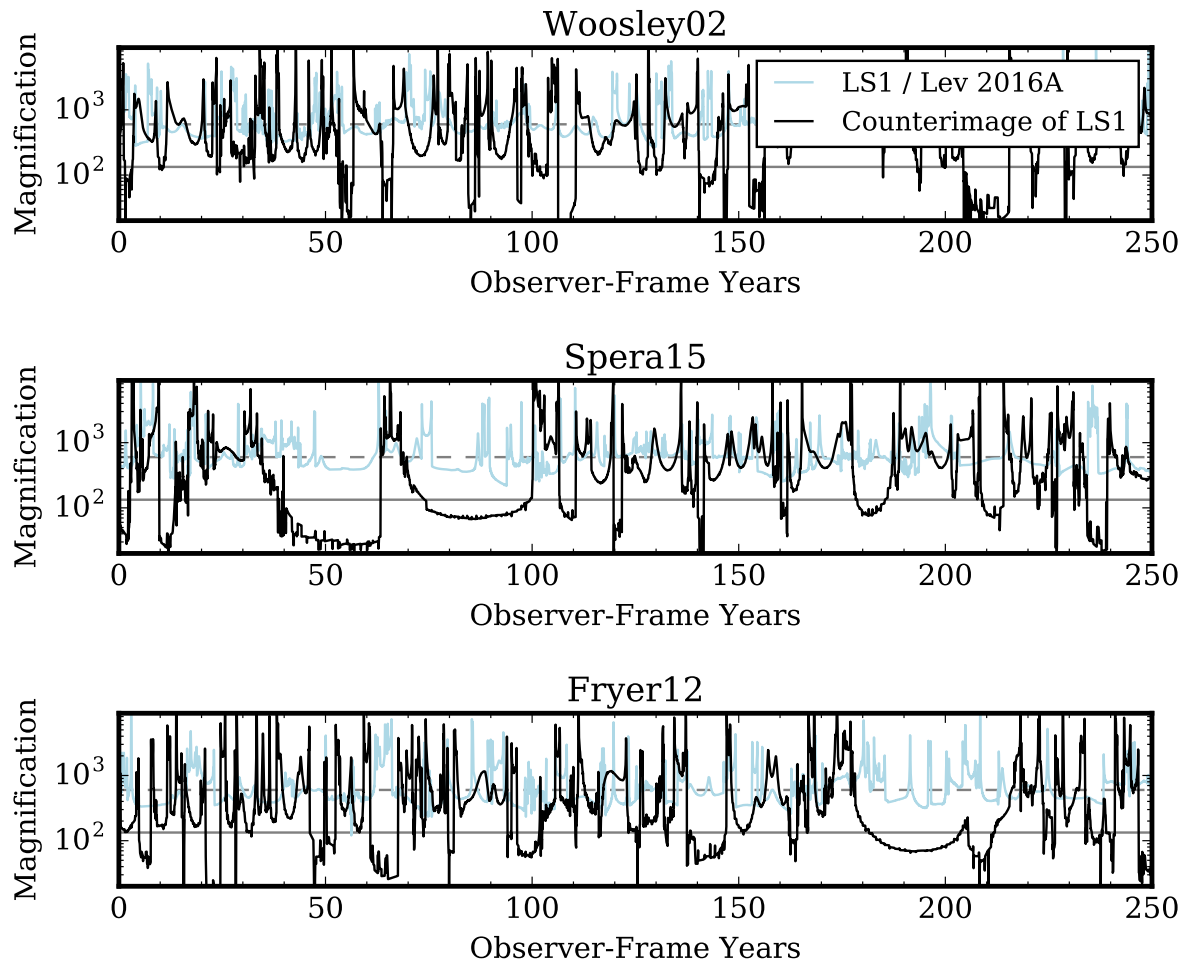


Fig. S6: Simulated light curves of a star at $\theta = 0.13''$ from cluster CC for three stellar evolution and core-collapse models. These include the solar-metallicity, single stellar evolution models (Woosley02) (20), as well as single stars at subsolar metallicity ($Z = 0.3Z_{\odot}$; $Z = 0.006$) where BHs with masses up to $30 M_{\odot}$ form from the collapse of massive stars (Fryer12) (21), and stars having initial masses greater than $\sim 33 M_{\odot}$ become BHs with masses within the range $20\text{--}50 M_{\odot}$ (Spera15) (22). For the Fryer12 and Spera15 models, the counterimage on the Lev 2016B side may travel through a region of relatively low magnification for decades owing to BH remnants of stellar evolution. The Woosley02 model yields significantly fewer decade-long intervals with low magnification. The simulated star has an apparent transverse velocity of 1000 km s^{-1} and a radius of $1000 R_{\odot}$, although only peaks are sensitive to the star’s size.

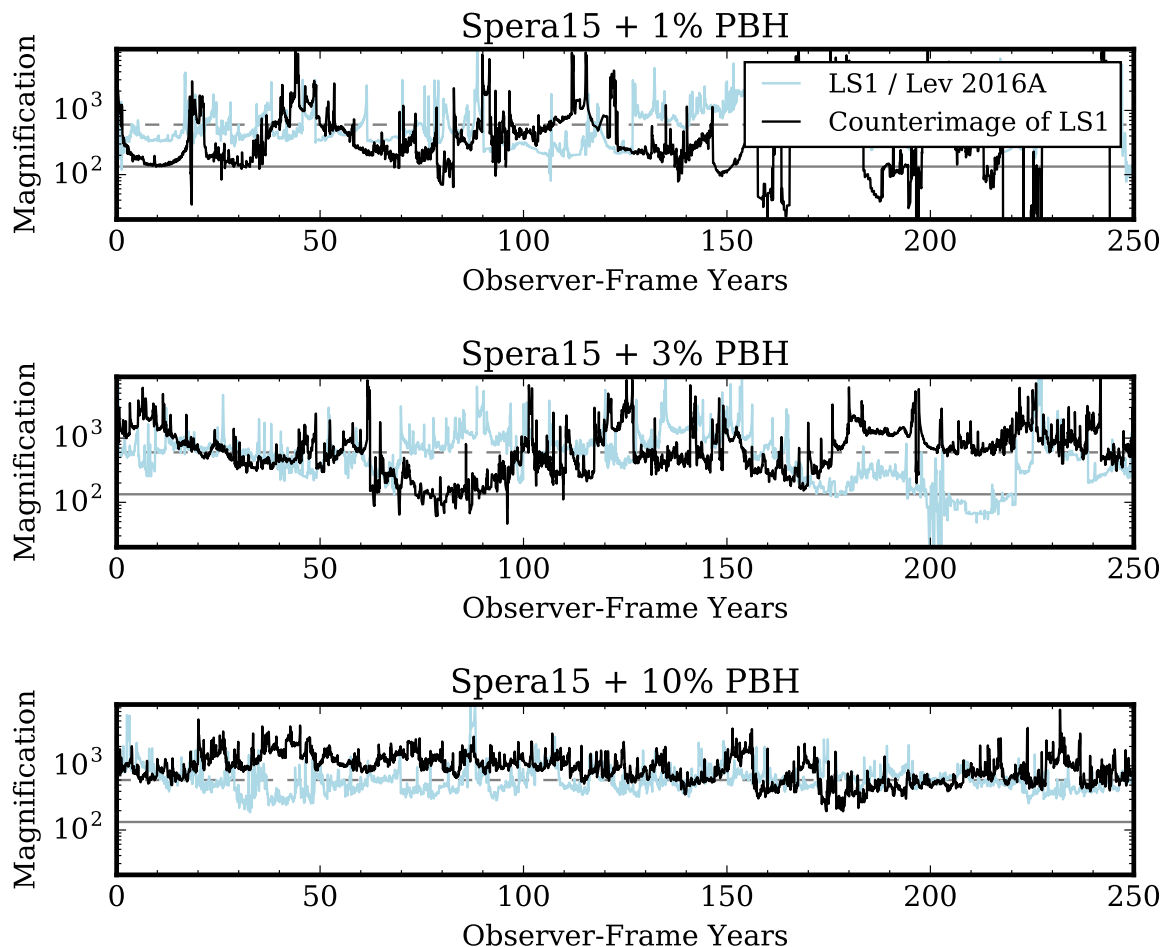


Fig. S7: Effect of increasing abundance of $30 M_{\odot}$ BHs on the simulated light curves of star at $\theta = 0.13''$. When PBHs account for no fraction of cluster DM (upper-left panel), the counterimage on the Lev 2016B side may travel through a region of relatively low magnification for decades owing to BH remnants of stellar evolution. Replacing 3.3% (upper-right panel) and, in particular, 10% (lower panel) of smooth DM with $30 M_{\odot}$ BHs yields light curves where hiding a counterimage for a decade becomes improbable. The simulated star has an apparent transverse velocity of 1000 km s^{-1} and a radius of $1000 R_{\odot}$. Only peaks in the light curve depend sensitively on the star’s size.

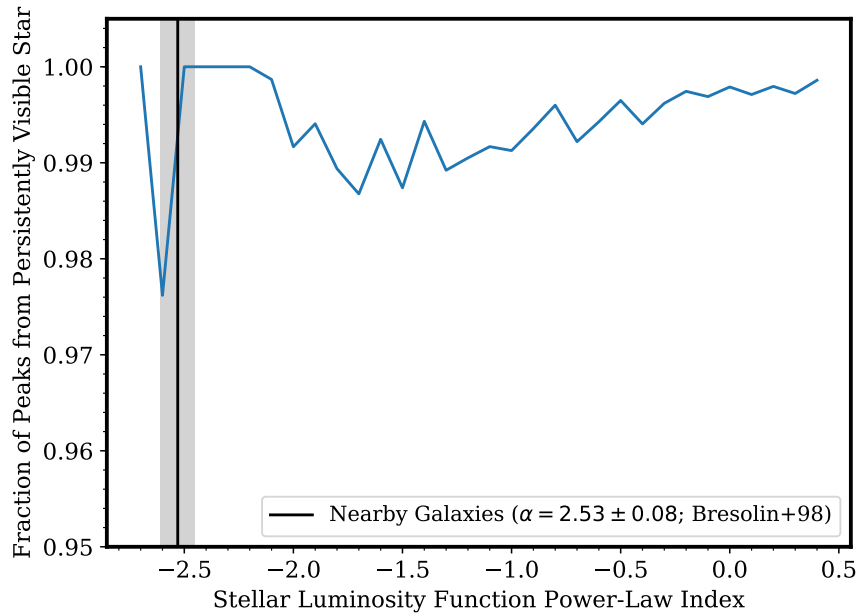


Fig. S8: When a lensed star has a bright average apparent magnitude ($F125W < 27.7$ mag), it will also be responsible for almost all bright microlensing peaks ($F125W < 26$ mag) observed near the CC for simple assumptions. Here we plot the fraction of bright peaks caused by the bright star against the index of the stellar luminosity function. Since $\gtrsim 99\%$ of events likely arise from the luminous star, it is likely that Lev 2016B corresponds to the same star as LS1. However, this simulation randomly assigns positions to massive stars; accounting for the observed clustering of massive stars in associations may show that the probability of Lev 2016B and LS1 corresponding to two separate events is greater than is indicated by this simulation.

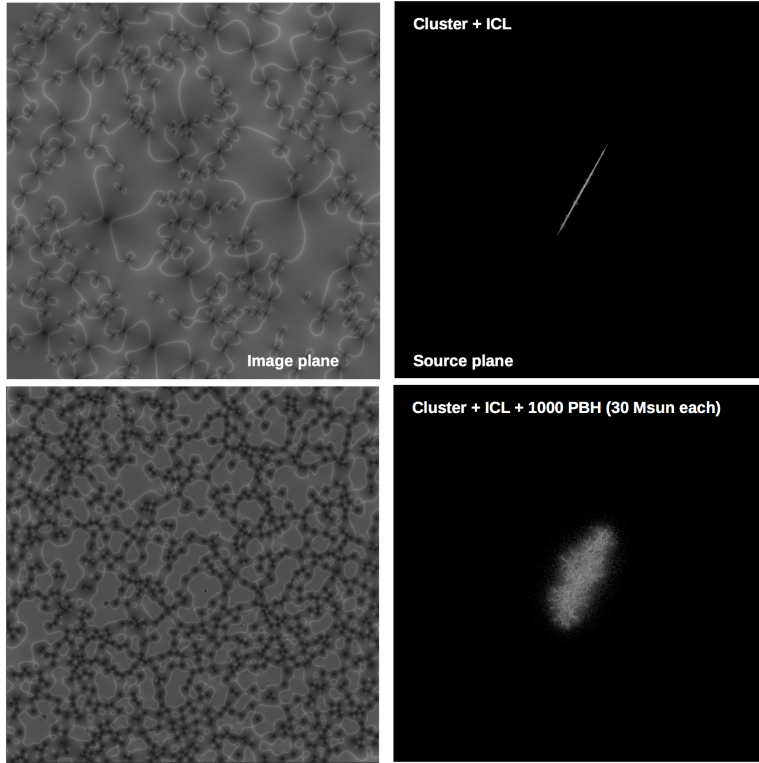


Fig. S9: Magnification maps in the image (left panels) and source (right panels) planes. The lens plane is populated with stars and compact object remnants to match the mass density in surviving stars and remnants we infer for the ICM ($6.3_{-3.3}^{+10.3} \times 10^6 M_{\odot} \text{ kpc}^{-2}$). In the lower panels, we show the effect of replacing 50% of the cluster DM with $30 M_{\odot}$ PBHs.

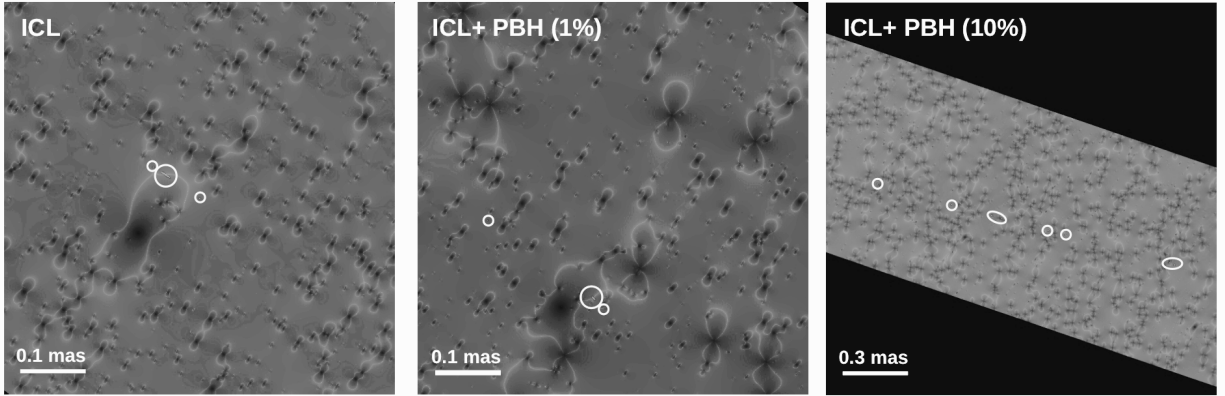


Fig. S10: Example of trains of counterimages that appear as lensed background star traverses region near the galaxy-cluster caustic. We show example of trains without PBHs (left panel), where $30 M_{\odot}$ PBHs account for 1% of DM (middle panel), and where $30 M_{\odot}$ PBHs account for 10% of DM (right panel). Increasing the PBH abundance yields more extended trains, although their extent (~ 3 milliarcsec) when PBHs account for 10% would be too small to detect in *HST* imaging. The simulation shown is of a $1000 R_{\odot}$ star whose image appears at an offset of $0.13''$ from the cluster CC. Near peak magnification, the star appears as a “train” of counterimages. Circles in right panel each enclose one part, and ellipses enclose two parts, of the train. In addition to replacing fractions of cluster DM with PBHs, we have populated the lens plane with stars and compact object remnants to match the mass density in surviving stars and remnants we infer for the ICM ($6.3_{-3.3}^{+10.3} \times 10^6 M_{\odot} \text{ kpc}^{-2}$).